remote sensing

MDPI

Article

An Analysis of Powder, Hard-Packed, and Wet Snow in High Mountain Areas Based on SAR, Optical Data, and In Situ Data

Andrey Stoyanov, Temenuzhka Spasova and Daniela Avetisyan *

Department of Aerospace Information, Space Research and Technology Institute, Bulgarian Academy of Sciences, Str. "Acad. Georgy Bonchev" Bl. 1, 1113 Sofia, Bulgaria; andreiIKIT@space.bas.bg (A.S.); tspasova@space.bas.bg (T.S.)
* Correspondence: davetisyan@space.bas.bg

Abstract: The following study presents the results obtained from a comparative analysis of dry (powder and hard snow) and wet snow based on satellite data and in situ data methods for monitoring in the high mountain belt of Bulgaria. The aim of the study is to analyze the effectiveness of different spectral indices based on satellite data from Synthetic Aperture Radar (SAR), high-resolution (HR) imagery, and spectrometer data for assessing the state and dynamics of the snow cover. The methods studied and the results obtained were validated by instrument-based field observations, with instruments using thermal imaging cameras, spectrometer measurements, ground control points, and HR imagery. Satellite data offer an ever-widening view of trends in snow distribution over time. All these data combined provide a detailed picture of surface temperature and snow properties, which are crucial for understanding snowmelt processes and the energy balance in the high-altitude belt. The findings suggest that a multi-method approach, utilizing the combined advantages of SAR satellite data, offers the most comprehensive and accurate framework for satellite-based snow cover monitoring in the high mountain regions of Bulgaria, such as Rila Mountain. This integrative strategy not only improves the precision of snow cover estimates but can also support many water resource-related studies, such as snowmelt runoff studies, snow avalanche modeling, and better-informed decisions in the management and maintenance of winter tourism resorts.

Keywords: SAR data; snow cover monitoring; thermal camera; spectrometer; high-resolution (HR) imagery

check for updates

Academic Editors: Livio Pinto, Niccolò Dematteis and Francesco Ioli

Received: 15 March 2025
Revised: 25 April 2025
Accepted: 28 April 2025
Published: 7 May 2025

Citation: Stoyanov, A.; Spasova, T.; Avetisyan, D. An Analysis of Powder, Hard-Packed, and Wet Snow in High Mountain Areas Based on SAR, Optical Data, and In Situ Data. *Remote Sens.* **2025**, *17*, 1649. https://doi.org/10.3390/rs17091649

Copyright: © 2025 by the authors. Licensee MDPI, Basel, Switzerland. This article is an open access article distributed under the terms and conditions of the Creative Commons Attribution (CC BY) license (https://creativecommons.org/licenses/by/4.0/).

1. Introduction

The high mountain belt in Bulgaria is a key research area in which snow accumulation and snow retention are of great importance and a primary focus. The accumulated snow cover in high mountain areas serves as water reservoirs, supporting important processes such as climate regulation, water resource management, ecosystem functioning [1], and the management of winter ski resorts in Bulgaria for tourism needs. Climate change affects the dynamics of snowpack formation, as rising temperatures lead to reduced snowfall, which reduces snow accumulation. Moreover, higher temperatures in winter and spring seasons cause earlier snowmelt, influencing the water supply [2]. These changes have cascading effects on ecosystems, water resources, and weather patterns at the local, regional, and global levels.

Traditional methods of snow cover monitoring in the high mountains are often limited by difficult-to-access terrain and harsh weather conditions in winter, which determines the use of modern technologies such as satellite data. Satellite observations offer large-scale

and regular snow cover monitoring, including in hard-to-reach and remote areas, providing valuable data on its dynamics and changes over time. Satellite imagery in the visible and infrared range of the electromagnetic spectrum is advantageous in identifying snow cover and distinguishing snow from other surfaces [3–6]. The utilization of visible (VIS) and near-infrared (NIR) or short-wave infrared (SWIR) bands to distinguish snow and clouds dates back to the mid-1970s [7–9].

The physical parameters of snow, such as snow moisture, which indicates the degree of liquid water content in the snowpack, along with snow density and snow water equivalent (SWE), are the most important parameters for many water resource-related studies, such as snowmelt runoff and avalanche modeling [10]. The traditional survey of these parameters is very expensive and difficult [11]. Optical remote sensing has been used effectively to map the snow cover area [12–16], snow moisture [4], and snow grain size with hyperspectral data [17,18]. Extracting the physical properties of snow using optical data remains a major gap due to topographic shading and the presence of cloud cover; therefore, in these cases, SAR offers a better alternative for estimating snow and glacier dynamic parameters, as shown in various studies [11,19–23] and discussed in the next section.

The advantage of the passive microwave method is that it detects the physical presence of liquid water in the snowpack—a parameter that is missing from surface air temperature data. The algorithm is validated using in situ observations from weather stations, snow pit measurements, and a surface-based passive microwave radiometer. The validation results indicate the algorithm has a high success rate for melt durations lasting multiple hours/days and where the melt event is preceded by warm air temperatures [24]. Spectral gradient ratios, including the Gradient Ratio (GR) [25] and Gradient Ratio Polarization (GRP) [26], were developed to exploit complementary information from different microwave frequencies and polarizations for rain-on-snow (ROS) detection. The passive microwave (PM)-based GRP approach was also observed to be effective in detecting ROS and associated winter melt events [26,27]. The algorithm does not reliably identify short-duration events or events that occur immediately after or before periods with extremely cold air temperatures due to the thermal inertia of the snowpack and/or overpass and resolution limitations of the satellite data [28].

According to the World Meteorological Organization (WMO), microwave remote sensing provides several advantages compared to other satellite sensors, as microwave data can provide information on the snow characteristics that are of most interest to hydrologists, i.e., snowpack area, snow water equivalent (or depth), and presence of liquid water in the snowpack which signals the onset of melt [29]. Snow on the Earth's surface is simply an accumulation of ice crystals or grains, resulting in a snow cover that can cover all or part of an area of the Earth [30].

Microwave imaging (SAR imaging) has advantages over visible and NIR imaging, where cloud penetration and solar independence are essential [31]. Microwave observations of snow are sensitive to changes in surface moisture and thus provide useful information about changes in its physical state. Conventional mid- and low-frequency SAR data (e.g., C-, L-channel) are useful for detecting and highlighting wet snow [23]. Discrimination of total (wet + dry) snow cover still remains a problematic research approach [23,32]. The full polarimetric SAR data contains more information than the corresponding single or dual polarization SAR data. Therefore, SAR polarimetry has great potential for mapping snow-covered areas, and analysis of SAR polarimetry data can be extremely useful for developing a methodology for distinguishing snow from other surface features. Radar backscatter from snow surfaces is influenced by various factors, mainly the dielectric profiles of the snowpack and the soil foundation, influenced by the snow grain sizes and their distribution in the snowpack, and the roughness of both the air-snow and snow–soil interfaces [33–36].

The application of SAR data for snow monitoring includes the selection of an appropriate polarization, which depends on the specific monitoring objectives and snow characteristics. Cross-polarization (e.g., HV or VH) is often preferred when observing snow, as it can provide better contrast between snow covers and other surfaces. When microwaves are backscattered from structurally complex surfaces such as snowpack, the signal obtained in cross-polarization often carries more specific information about the surface features [37–39]. Cross-polarized data are significantly useful in mountainous regions with steep topography, where, due to the moderate angular dependence of backscatter, cross-polarized data separate the wet snow and snow-free surfaces better on fore-slopes. For co-polarized data, this separability decreases significantly, especially towards low incidence angles [39]. Co-polarized images are suitable for studies of the physical properties of the snow cover, such as snow depth, humidity, and density [40,41].

Another range of the electromagnetic spectrum in which snow cover can be successfully distinguished is the thermal range with wavelengths λ = 11–13 μm [42]. Spectral contrast is enhanced when the snowpack evolves from a type of disaggregated snow, such as fine snow or medium and coarse melt forms, to welded snow, such as sun crust and bare specular ice [43–45], which is often used to verify data from the area of interest. The thermal camera can be used to make inferences about the thermal conductivity of snow or to analyze the way heat passes through the observed snow mass.

The remote sensing of snow cover is also performed through field data sampling using a mobile spectrometer, which usually provides more accurate data. The resulting spectral data can be summarized as spectra of the energy reflected from different objects. The brightness of objects in the spectral range below 3 μm is determined by their ability to reflect and scatter the electromagnetic energy incident on them [46]. Upon the spectral curves obtained from a spectrometer, it can be guaranteed that real objects have been observed, in this case, the different types of snow. In addition to the generated indicators and statistics, there is also an objective assessment of the field operator.

Snow has properties characteristic of both liquids and solids. Which of these properties prevails depends on the density of the snow (for wet snow between 100 and 300 kg/m^3, for solid between 300 and 500 kg/m^3 and between 30 and 100 kg/m^3 for powder snow), the type of crystals, the water content, and, most of all, on the temperature. The powder snow is formed at low temperatures (usually below −5 °C), contains less than 3% water, and has a high albedo. The exact opposite of it is wet snow, which is characterized by a higher temperature up to 0 °C and a water content of 3% to 8%, which makes it heavy.

The aim of the study is to compare SAR satellite data for monitoring snow cover in the high mountain belt of Bulgaria, assessing their effectiveness, accuracy, and applicability with in situ data collected for the three types of snow. The study analyzed the performance of SAR indices, including cross-polarized VH data and co-polarized VV data in ascending and descending orbits. To achieve this goal, a selection of suitable sites and a selection of suitable satellite data with different spectral characteristics, together with in situ data measurements (Section 2), have been analyzed. A multi-method approach for processing and combining data has been applied in order to study the spatial distribution of three types of snow. A model of the applied methodology has been built, and an interpretation of the obtained results has been made.

The study mainly focuses on the opportunities that field data provide for validating derived SAR data results. The field data were collected from the Borovets test site located in Rila Mountain, Bulgaria, and data from the Sekonic C-800 mobile spectrometer, (made in Japan, distributed by Sekonic Corporation, Denville, NJ, USA), with a wavelength of 380 to 780 nm and a thermal camera with a wavelength of 8 to 14 μm were used [47–49].

A major contribution to the field data obtained from the spectrometer is the measured color temperature values, known as Correlated Color Temperature (CCT), indicating how yellow or blue the color of the light emitted by a light source appears. The CCT range, measured in Kelvins, is always between 2700 and 6500 degrees [50]. The color is "warmer" and more red or orange at the lower end of the scale. On the other hand, the higher end of the spectrum has a "colder" color and leans more towards white or cool blue, where objects such as snow should fall. Of no less importance is the CRI (color rendering index), which is described in detail together with CCT in Section 2, Materials and Methods.

For the purposes of this study, all points from in situ surveys were further grouped into three groups: powder snow, hard-packed snow, and wet snow. Powder snow is soft and loose, meaning it falls easily through the fingers and usually cannot be compacted [51]. It is dry snow that occurs when the surface air temperature is below freezing [52]. Hard-packed snow could be described as the opposite of powder snow. It refers to snow that has gone through a cycle of melting and refreezing, resulting in a hard and icy crust on top of the snowpack [51]. The wet snow is very moist and dense snow that forms when air temperatures are around or above freezing [52,53]. This type of snow is less affected in the study, as it was measured in very few locations during the field surveys.

2. Materials and Methods

2.1. Study Area

The study area encompasses one test site named after the resort of Borovets, situated in the highest mountains of the Balkan Peninsula, Rila (Figure 1). The test site is situated between 1254 m and 2905 m above sea level and covers an area of 53 km^2 in Rila Mountain. The area of the test site, Borovets, includes parts of the Central Rila Reserve, and both sites include numerous protected areas and habitats. The greatest part of the test site is covered by *Pineta mugi* formations (16.8 km^2) and acidophilic psychrophytic grass (*Carticeta curvulae*, *Festuceta riloensis*) and shrub (*Saliceta herbaceae*) communities (16.7 km^2). The areas of the spruce forests (*Piceeta abietis*) are also relatively large (8.2 km^2) [54].

In the high mountain belt of the Rila Mountains—above 2000 m altitude—the snow cover is thickest in March—70–80 cm. In the highest parts, the maximum thickness of the snow cover reaches 200–240 cm. The average duration of the period with stable snow cover at an altitude above 2000 m reaches 180–200 days [55].

2.2. Data and Processing of Various Data Types

Data from satellites and the field sensors used in this study are described in Table 1. The model of methodology of processing and analysis of the selected 3 types of snow, powder, hard-packed, and wet, is presented in Figure 2, including the main data types and indices used.

2.2.1. SAR Data

In the present study, microwave SAR imagery from the Sentinel-1 mission of the Copernicus Programme was used. The Sentinel-1 mission is the European Radar Observatory for the Copernicus joint initiative of the European Commission (EC) and the European Space Agency (ESA). The mission comprises a constellation of two sun-synchronous polar-orbiting satellites, sharing the same orbital plane with 180° orbital phasing difference, performing C-band Synthetic Aperture Radar [SAR] imaging at the central wavelength of 5.405 GHz, corresponding to 5.55 cm. It operates in four imaging modes with different resolutions (down to 5 m) and coverage (up to 400 km). It provides dual-polarization capability, very short revisit times, and rapid product delivery. Sentinel-1 data have a

spatial resolution of 10 m in both VV and VH polarizations. The Interferometric Wide (IW) swath mode is the main acquisition mode over land surface [56] (Table 1).

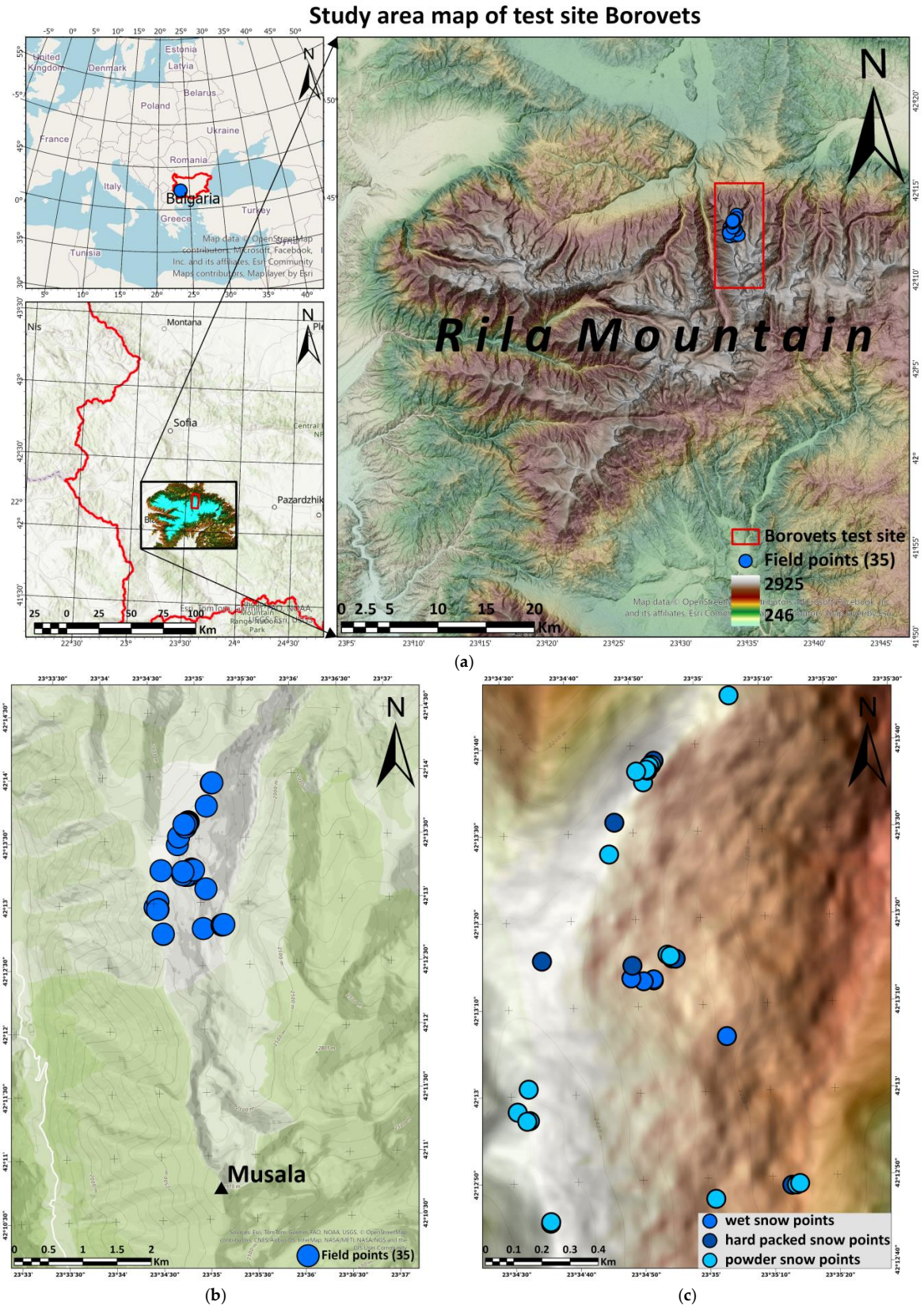

Figure 1. Location of the test site of Borovets. (**a**) Map of the test site, Borovets. (**b**) Map with field points of the test site Borovets. (**c**) Map with 3 types of snow.

Table 1. Satellite and in situ data acquisition dates.

Satellite	Date	Spectral Band, Wavelength	Spatial Resolution
Sentinel-1-A	5 March 2024 11 March 2024	λ = 5.6 cm, C band Polarization: VH, VV	10 × 10 m
PlanetScope	4 March 2024	Coastal Blue—443 nm Blue—490 nm Green I—531 nm Green—565 nm Yellow—610 nm Red—665 nm Red edge—705 nm NIR—865 nm	3 × 3 m
Sekonic C-800 mobile spectrometer	4 March 2024	380 to 780 nm	1 nm
HT-19 thermal camera	4 March 2024	8 to 14 μm	320 × 240 Pixels

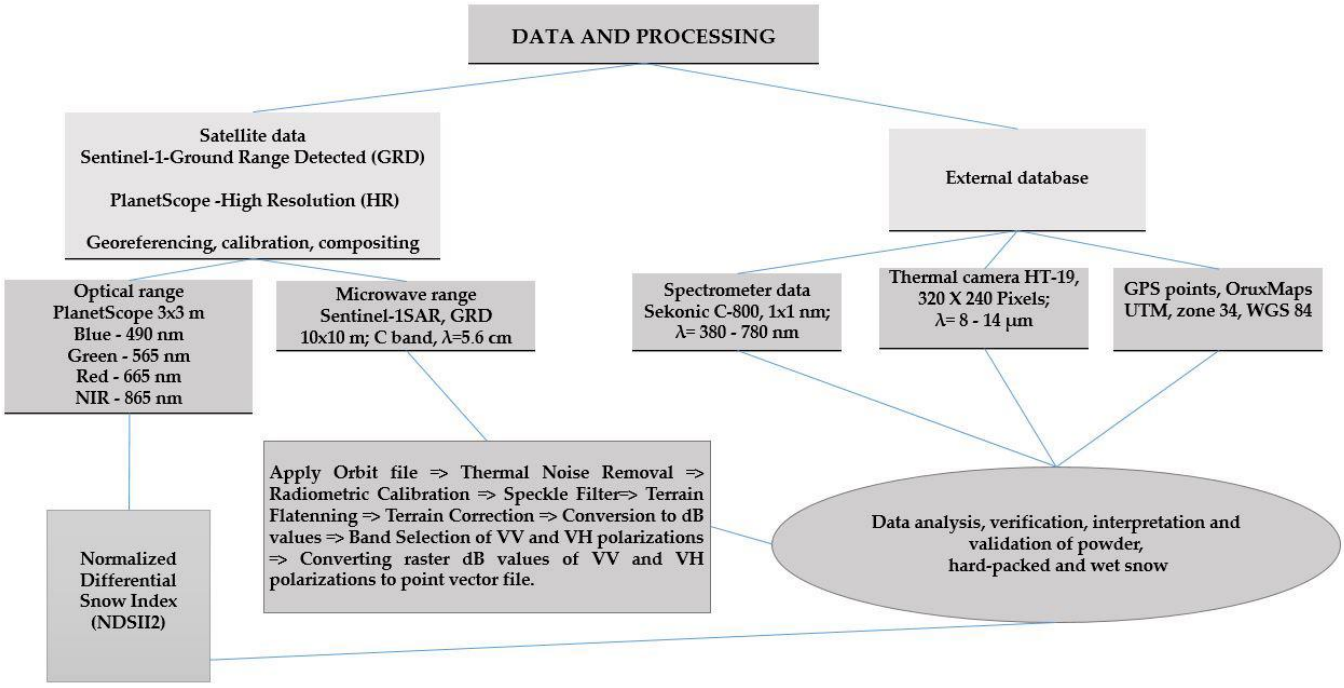

Figure 2. Model methodology for analysis of powder, hard-packed, and wet snow.

Sentinel-1 has a side-looking imaging geometry, so images are subject to geometry-induced radiometric distortions (shadow, layover, and foreshortening effects). In the case of foreshortening, mountain slopes facing the sensor are compressed into a few image pixels, which appear bright. The layover effect, being an extreme case of foreshortening, occurs in cases where the top of the mountain is closer to the sensor than the bottom. Radar-shadowed areas correspond to the hidden parts of the radar beam. Layover, foreshortening, and shadow regions are usually simulated using digital elevation models and sensor acquisition parameters [57–59]. These characteristics of the SAR images require specific pre-processing operations, which should be implemented to reduce distortions caused by landscape and sensing angle leading to foreshortening, layover, and shadow effects, thus enhancing the accuracy of the results obtained. In addition, the resultant speckles caused by phase interferences reflected from countless ground features can degrade the image quality significantly [60]. In the present study, the Terrain Correction operation, with a

DEM of 30 m resolution, is a part of the applied workflow and is used to minimize the geometric distortions caused by the side-view imaging of the SAR sensor. In addition, both SAR data acquisition orbits are used to reduce, as much as possible, radar shadow effects and topographic effects of the rigid mountain terrain. Radar shadow, layover, and foreshortening masks are created in SNAP software (Version 10.0.0) [61,62] by "SAR simulation" in the radar toolbox, showing the areas not affected by (SAR signal) geometric distortions [63]. The following analysis of the obtained results aims to find the pros and cons of SAR data from ascending and descending orbits for the selected test sites in order to be applied or to be useful for the creation of future monitoring models over the mountain area of the Rila range.

Sentinel-1A Level-1 Ground Range Detected (GRD) products in the Interferometric Wide Swath mode, in dual polarization of VV and VH from both ascending and descending orbits, were used in the present study [64]. For the test site area, SAR data from 5 March 2024 in ascending orbit and 11 March 2024 in descending orbit were used. In ascending orbit, the satellite moves from south to north and passes over the area of interest in the morning hours, and in descending orbit, the satellite moves from north to south and passes over this area in the afternoon/evening hours. The acquisition dates for all orbits do not match, and the closest available data are used to obtain SAR data from both orbits. All this leads to obtaining data with a higher temporal resolution of 5–6 days [65]. According to climate data, it is assumed that no significant changes (snowfall or avalanches) were observed in the snow cover dynamics during these 6–7 days, with the reference date being 4 March 2024. The choice of time for conducting field studies often does not coincide with the day of the satellite transit.

Both types of orbits are used to compare the results regarding different sensing angles of each orbit at data acquisition and thus to extract more information about snow cover distribution from SAR imagery. SAR backscatter coefficients at the C-band, converted to decibel values, were used for further analysis. SAR images are freely available on the Copernicus Data Space Ecosystem [64]. All the radar images were downloaded and processed in a GIS environment—SNAP, developed by ESA [61], and ArcGIS Pro, developed by ESRI [66].

SAR imagery processing includes several operations before data analysis: Apply Orbit file => Thermal Noise Removal => Radiometric Calibration => Speckle Filter => Terrain Flattening => Terrain Correction => Conversion to dB values (all of these steps are performed in SNAP software—Version 10.0.0) => Band Selection of VV and VH polarizations => Converting raster dB values of VV and VH polarizations to point vector file (are performed in ArcGIS Pro 3.0.1). The spatial resolution of the SAR imagery used in the present research is upsampled to 10 m. The coordinating system of the radar data are set to UTM zone 34N.

2.2.2. High-Resolution Data from PlanetScope

High-resolution (HR) satellite data from PlanetScope were used as part of the validation process. PlanetScope, operated by Planet, is a constellation of approximately 130 satellites able to image the entire land surface of the Earth every day. Satellite images of PlanetScope have a spatial resolution of 3 m. Since their first launch in 2014, they have released three PlanetScope instrument types: Dove Classic, Dove-R, and SuperDove [67]. SuperDove instrument images consisting of 8 spectral bands (Table 1) were used in the present study for validation/verification purposes. PlanetScope images from 4 March 2024 were used for the test site. The pre-processing steps for the HR images include clipping the imagery to the areas of interest and visualization enhancement with the ArcGIS Pro 3.0.1 software [66]. The coordinating system of the HR data is set to UTM zone 34N (Table 1).

2.2.3. Field (In Situ) Data

To assess the snow cover condition and validate remote sensing data, in situ surveys were conducted, and points with different snow cover characteristics were collected from the test site area. About 35 profiles, GPS coordinates (Figure A1), and images were generated (by a mobile thermal camera and a field spectrometer). Validation of the SAR data in this article was performed with test profiles from 4 March 2024, which determines the use of available SAR and optical imagery as close as possible to this referring date. These profiles were generated in the high mountain belt, above 1700 m altitude, due to the possibility of measuring different types of snow: powder snow, wet, and hard-packed snow.

Mobile Spectrometer

Spectrometric measurements using Sekonic C-800 for the ground surface were also part of the remote sensing in this study and were performed at a measurement height of less than 50 cm. This way, the spectrometer is as close to the object as possible, and the area is significantly smaller, which results in much more detail being provided for the snow objects studied. This is important in the interpretation of data from spectrometric measurements since one or more objects may fall into the instantaneous field of view. The registration of details in the spectral reflectance characteristics of the objects depends on the spectral resolution and is of particular importance in the study of minerals and rocks, water, snow, and ice.

Besides the spectral distribution of natural light in the visible spectrum, the data for each spectral profile contains its originally generated number and Correlated Color Temperature (CCT) measured in Kelvins [K] (Figure A2), CRI Ra, CRI (R1-R15), CIE1931 x, CIE1931 y, Hue, saturation, and TM-30-18 for point 1 (Table A1, Figures A2 and A3). The color rendering index (CRI) is a quantitative measure of the ability of a light source to faithfully reproduce the color of various objects compared to an ideal or natural light source [68]. The color rendering index reflects the effect of a luminaire on the color of illuminated objects. Simply put, CRI measures how well a luminaire reproduces the illumination of sunlight, which has a perfect CRI of 100. A color rendering index of 100 means that colors appear exactly as they should [68,69]. When discussing CRI, it is best to use the term "CRI (Ra)" or general CRI, which covers colors from R1 to R8. When discussing extended CRI, the term "CRI (e)", "Re", or extended CRI is used and covers colors from R1 to R15 (Table A1), with a demonstration of the values of these parameters (Figure A2) [68].

The Correlated Color Temperature (CCT) for this product ranges from 1600 to 40,000 Kelvins [K]. The CCT determines the color, not the brightness of the light source. CCT is the expression that defines and categorizes the color of a light source. Color temperature indicates the color of visible light emitted by a light source [70]. There are 3 groups of objects according to the light colors. These are objects that reflect the incident light in warm white color, natural white color, and cool white color. The range of 2700–3500 K is warm white, the range of 3500–4500 K is natural white, the range of 4500 K–6500 K is described as cool white [70,71] (Figures 3 and 4), and it is predominant in this study.

In Figure 4, the CCT values for test site field points are shown. ID 1 to ID 5 are values for wet snow, ID 6 to ID 15 for hard-packed snow, and ID 16 to ID 35 for powder snow.

The color coordinates xyz are used for objects of mixed class. To determine the color, it is enough to know x and y. The color coordinates (x, y) are a color characteristic that is used in the study of natural objects. In this spectrometer, the color coordinates xy are determined relative to the standard irradiance D65 in the CIE 1931 system (Table A1).

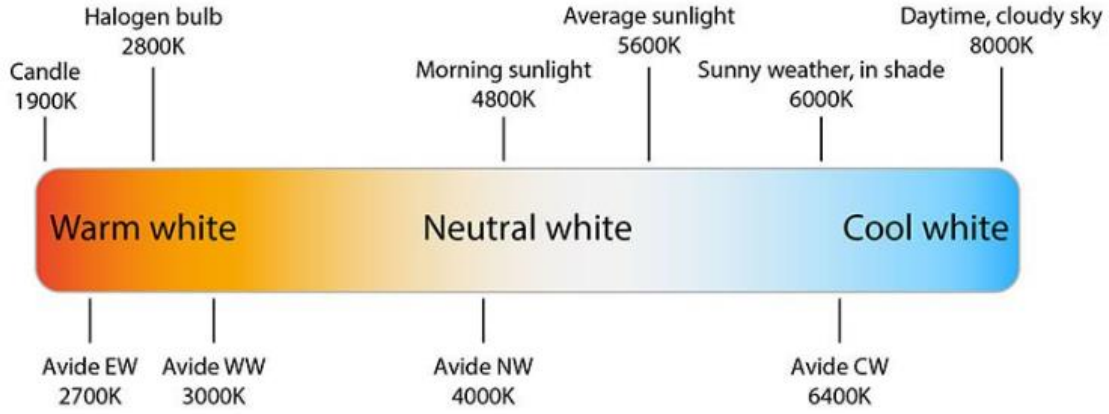

Figure 3. Correlated Color Temperature (CCT) in Kelvin [K] of field points from the test site Borovets.

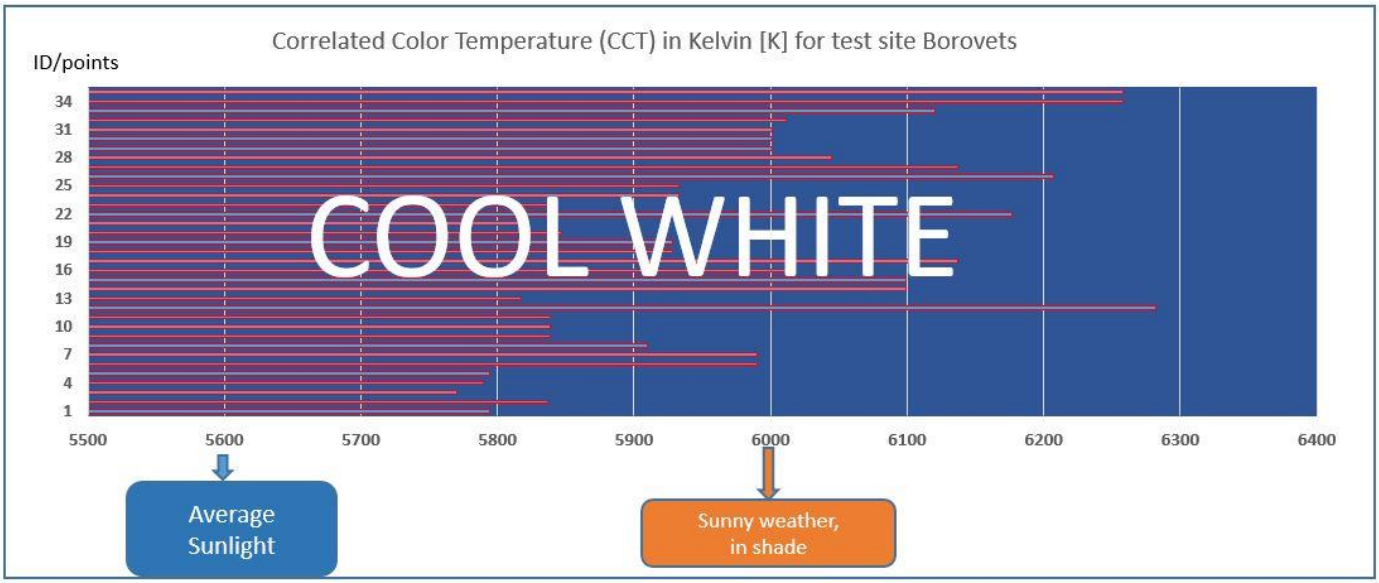

Figure 4. The most widely used Correlated Color Temperature (CCT) range and Kelvin temperature chart [71].

Saturation determines the brightness and intensity of a color [72], and Hue is one of the basic properties (called color appearance parameters) of a color, technically defined in the CIECAM02 model as "the degree to which a given stimulus can be described as similar to or different from stimuli that are described as red, orange, yellow, green, blue, violet" within certain theories of color vision [73].

The Rf metric is similar to the CIE CRI "CRI" value, an average of the test-light-to-sunlight color fidelity disparities for the 99 test samples. The differences are judged on a 100-point scale, with the higher numbers indicating the ability of the test light to generate colors closer to sunlight [74] (Figure A3).

The Rg metric represents the other important factor for human perception of color: saturation. It is also an average of the disparities between test light and sunlight. It is based on a baseline score (100)—higher scores (100–140) indicate higher saturation (on average), and otherwise lower scores (60–100) indicate undersaturation [74] (Figure A3).

Color Vector Graph

The Rg metric is a number that reflects overall under- or over-saturation but does not indicate which color areas are problematic. The TM-30-15/30-18 remedies this with a superimposed circular vector graph over a color space, representing where color saturation

anomalies occur. Note that the CAM02-USC color space is a 3D space, but it has been "flattened" to show the shifts in the saturation dimension [74] (Figure A3).

The ANSI/IES TM-30 standards are an internationally accepted set of guidelines for characterizing the color rendition (color rendering) performance of virtually any light source [75]. In 2018, IES issued an update to the TM-30: TM-30-18, which expanded on the original TM-30-15. TM-30-18 offers a more comprehensive evaluation of color quality. TM-30-18 is now widely accepted as the solid-state lighting color rendition standard and reporting format. The more recent TM-30-20 standard provides detailed guidance on the calculations to be used for objective characterization of light sources but retains the TM-30-18 report format [75] (Figure A3).

The spectral distribution of natural light is from 380 to 780 nm. In the generated spec-tral profiles, the following color ranges and wavelengths of the visible light spectrum in nanometers have been studied, which, for this type of spectrometer are as follows: violet ~380 nm to 420 nm, blue ~420 nm to 470 nm, cyan ~470 nm to 520 nm, green ~520 nm to 565 nm, yellow ~ 565 nm to 590 nm, orange ~590 nm to 640 nm, red ~640 nm to 740 nm, and near-infrared area above 740 nm [76]. A CSV file is available for each profile, generated via the software product, which is freely available on the Sekonic C-800 webpage [77].

In addition to the spectral profiles, a photograph was taken of each snow-type object to ensure the authenticity of the spectral curve. GPS coordinates for north latitude, east longitude, and altitude were taken using the OruxMaps mobile application, V.7.4.26 [47] in offline mode. Each of the photos generated by the application has a date and time, which is useful in the analysis and interpretation of the results (Figure A1).

Mobile Thermal Camera

The mobile thermal camera HT-19 was also used in the field research. It works in wavelength of 8–14 μm (Table 1), measurement accuracy ±2 °C, and 5 color scale palettes (Rainbow, Iron Red, Cold Color, Black and White, or White and Black), which makes readings more useful and easier to visualize because there is an excellent integration of surface temperature and real-time thermal imaging. The Iron Red color palette was chosen for the studies conducted, with the measured parameters being the maximum and minimum values of the ground temperature. The display also shows the central point temperature, which was taken into account when assessing the snow condition.

A typical feature of spectral snow emissivity is seen at wavelengths λ = 11–13 μm, where the emissivity has a spectral contrast with a local maximum at λ = 10.5 μm and a local minimum at λ = 13 μm [44]. All this scientific evidence about the spectral capability of snow was supported by the use of the mobile thermal camera, which also measures in the same spectral range. In this way, we obtained visual information about temperature differences on surfaces in real time, which helped in the analysis of data obtained from satellites.

2.3. Methods

After processing the satellite optical and SAR images, NDSII (Normalized Difference Snow Ice Index) and SAR dB values (for both polarizations and both orbits) were calculated, and the resulting values were extracted at the field observation points. The final step consists of validating the results obtained for each of the points with the field observation data, supported by field (in situ) measurements with a field spectrometer and a thermal camera, and HR images. Section 4 provides a comparative analysis and presents the advantages and disadvantages of each data type and corresponding methods for remote sensing of snow cover.

2.3.1. Remote Sensing Methods for Analysis of Powder, Hard-Packed, and Wet Snow Monitoring Based on SAR Data

Wet and dry snow behave differently in SAR imagery due to their penetration characteristics. SAR signals can penetrate the snowpack with depth depending on the wavelength of the signal. C-band SAR has a potential penetration depth of around 20 m when observing dry snow [78]. Since the grain size of snow is between 0.1 and 0.3 mm, the SAR signal, with its much longer wavelengths, passes through the snow crystals, preventing any kind of backscattering reflection from the snow crystals from being registered [79,80]. When the snow cover begins to melt, the dielectric properties of the snow cover change, significantly reducing the penetration depth to about 3 cm, and the backscattering reflection from the liquid water becomes the dominant component [78,81,82].

The radar backscatter values in the SAR imagery are in a linear scale and span a vast range of signal intensities when monitoring snow cover. In order to compress the large range of signal intensities into a more comprehensible scale of values, a logarithmic transformation into decibel (dB) values is needed. The dB values can effectively represent the large dynamic range of the SAR signal, allowing for a more precise detection of subtle changes in snow cover. The dB scale enhances the detection of anomalies in snow cover, such as snowmelt or accumulation of new, fresh snow cover, by highlighting changes that are less noticeable on a linear scale. This advantage of the logarithmic scale of representation is significant for climate studies and hydrological forecasting.

In the present study, the linear values of the SAR data are converted into dB values of VV and VH polarizations from ascending and descending orbits to compare and highlight their advantages and disadvantages for monitoring snow cover in different states.

2.3.2. Remote Sensing Methods and Indices for Analysis of Powder, Hard-Packed, and Wet Snow Based on Optical Data

In the present study, satellite optical data were used for the creation of RGB-composites and the calculation of NDSII in order to obtain information about the spatial distribution of the snow cover in the selected test area to be highlighted and extracted, and for validation purposes with the in situ data.

Normalized Difference Snow Index (NDSI)

The Normalized Difference Snow Index (NDSI) is the most used index for snow cover mapping. It represents the normalized difference in two bands, one in the visible and one in the short-wave infrared (SWIR) parts of the spectrum (Equation (1)). Snow cover has high reflectance in the visible part of the electromagnetic spectrum and high absorption in the NIR or SWIR, whereas the reflectance of most clouds remains high in those parts of the spectrum, allowing good separation of most clouds and snow [83]. In practice, the NDSI values for areas covered by snow range from 0.0 to 1.0. When the snow is registered by the sensor, the NDSI will be >0. The generally accepted NDSI threshold value used to determine snow cover distribution is 0.4, although many researchers suggest the NDSI can be set for particular situations with methods of threshold selection based on visual inspection/interpretation, empirical relationship, or automated selection [84]. The formula for the calculation of NDSI is as follows:

$$\mathrm{NDSI} = \frac{(\mathrm{Green} - \mathrm{SWIR})}{(\mathrm{Green} + \mathrm{SWIR})} \quad (1)$$

Since Planetscope imagery does not have spectral capabilities to provide satellite data in the middle infrared range of the electromagnetic spectrum (SWIR band), the presented research utilizes NDSII2 as the values and results regarding snow cover spatial distribution are very similar to those of NDSI. The authors propose the use of NDSII2 when data in the

spectral range of the SWIR band are unavailable, as Hall et al. suggested, since both indices are almost identical [16].

Normalized Difference Snow Ice Index-2 (NDSII2)

The Normalized Difference Snow Ice Index-2 (NDSII2) was developed by Dozier J. [15] in 1989 as a B2-B4 index of Landsat 5 TM for snow mapping, where B2 and B4 represent green and NIR bands of the sensor, respectively. It was used by Hall et al. in 1995 and Teleubay et al. in 2022 as a method to detect snow and ice areas [16,85].

It is calculated by using the visible green and near-infrared band combination (Equation (2)) in Erdas Imagine 2015 software [86], where the given name NDSII2 was taken from. The difference between NDSII and NDSII2 lies only in the name, depending on the sensor used, not in the equation, as NDSII is usually adopted for Landsat and MODIS sensors. Although the NDSII2 is designed for distinguishing snow and ice cover, in the present study, it was used to delineate snow cover using the high-resolution image bands from PlanetScope. The obtained results from the applied index were used for validation purposes.

$$NDSII2 = \frac{(Green\ [565\ \text{nm}] - NIR\ [865\ \text{nm}])}{(Green\ [565\ \text{nm}] + NIR\ [865\ \text{nm}])} \quad (2)$$

2.3.3. Verification

Field (in situ) data helps distinguish snow from other objects such as the sky, the sun, various infrastructure objects, etc., and also attempts to distinguish dry from wet snow. The snow in each point has different physical parameters and continuous dynamics that lead to the constructive or destructive metamorphosis of snow [63] (Figures 5, A4 and A5). The spectral reflection values between 700–760 nm are in the highest range, from 0.48 to 0.58, for the three types of snow. The lowest values are for wet snow and the highest for powder snow (Figures 5, A4 and A5).

The methodology of field (in situ) studies implies that they are carried out synchronously [87,88], as they cover three types of data generated at the same time for each of the sites. This means that when taking GPS coordinates, a photo is taken by a mobile application, a measurement is made in parallel by a spectrometer, and immediately after that, a photo is taken by a mobile thermal camera of the surroundings around each specific point. All these data validate the results obtained from the satellite images for the presence of snow. On the other hand, they help interpret the received information and, above all, give a clear idea of the physical condition and type of snow when analyzing satellite data with lower spatial resolution. Due to the lower spatial resolution of the satellite images, some of the pixels where the field studies were performed are mixed with vegetation. For that reason, in the interpretation of the results obtained applying satellite remote sensing methods, the points falling in mixed pixel areas were given different names from those in the field studies.

The use of in situ data from the Sekonic C-800 mobile spectrometer for the needs of this type of study has already been tested by the authors for in situ measurements in Antarctica, and the usefulness of this type of data validation for sites of interest has been demonstrated. Spectral reflectance distribution can be used as a qualitative indicator when analyzing the condition of snow [89]. The mobile spectrometer examines objects from a very close distance, in the 380–780 nm range of the electromagnetic spectrum. It is necessary to determine the distance from the object to the input optics, and, in this case, the distance is ~50 cm or less than 50 cm. In this way, a more detailed spectral curve of the object is available in the visible range for the individual colors of the electromagnetic spectrum, where the data from the different color ranges of the selected points can be clearly compared [90].

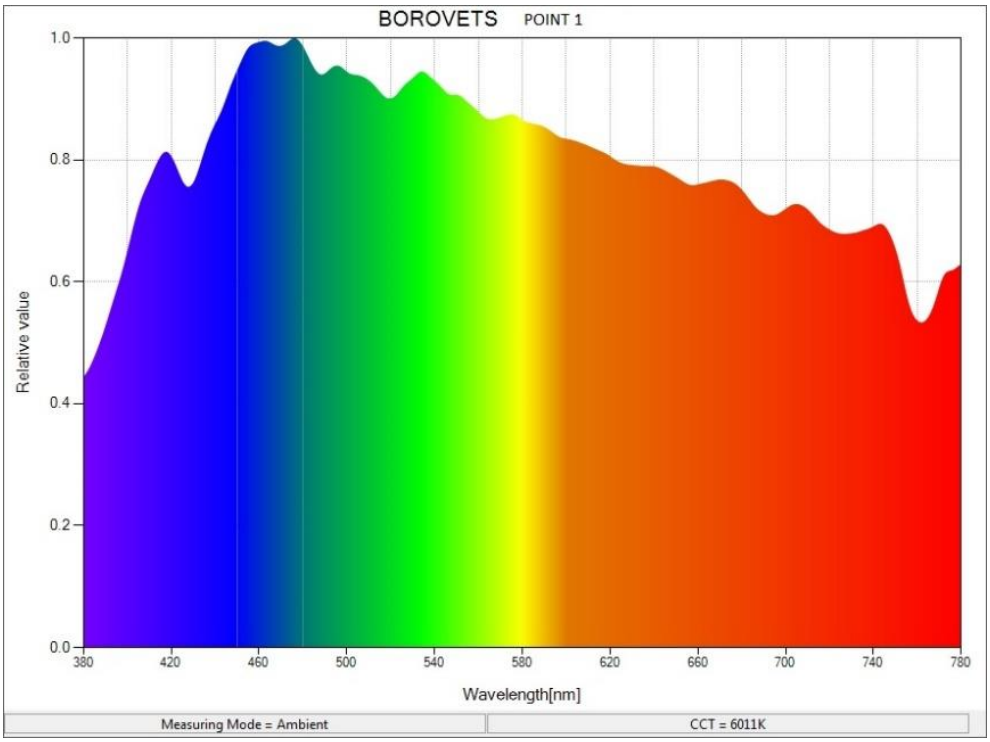

(**a**)

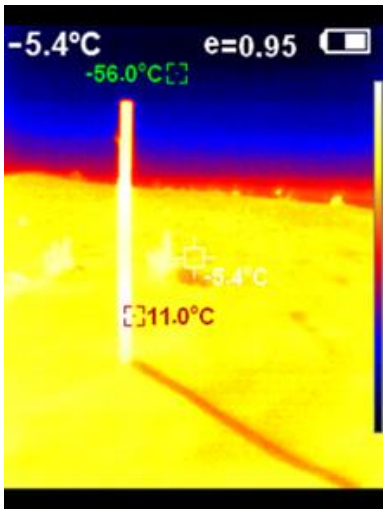

(**b**)

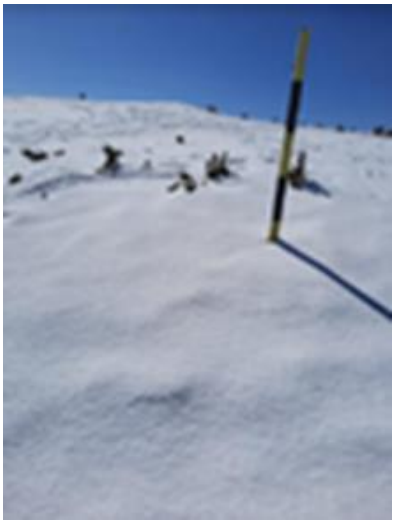

(**c**)

Figure 5. Powder snow, point 1. (**a**) Spectral reflectance curve of the powder snow, Sekonic C-800 mobile spectrometer. (**b**) Thermal image of the area of interest around the survey point, time 14:31:09, HT-19 thermal camera. (**c**) Photo of the powder snow of the area of interest around the survey point.

The spectral curves of objects can ensure that real objects and events are observed, in addition to the many indicators and statistics generated, which are easily validated. The objective assessment of the field operator is available, which can also validate what is seen through a field photograph. It is mandatory to add information on atmospheric conditions of measurement (atm) in field spectrometric measurements [90]. Monitoring by the spectrometer involves remote sensing, particularly when conducting field studies in different conditions and maintaining a distance of less than 50 cm from the object to the input optics or measurement height.

As a result of the processing of the primary spectral data measured using the Sekonic C-800 spectrometer, the spectral reflectance coefficient and spectral reflectance characteristics of the different types of snow in each of the visible bands or ranges of the electromagnetic

spectrum have been obtained. A detailed selection of the obtained spectral reflection characteristics of snow was made in order to create a database. The generated database also contains additional information on the type of surface to be surveyed, its structure, the area of profile collection (e.g., altitude), and the field spectrometric measurements performed with the above indicators and indices from the in situ survey points.

The type of spectral reflectance characteristics and their features are used in snow recognition. A characteristic feature of the spectral reflectance characteristics of snow is the high values of the spectral reflectance coefficient in the visible blue and blue-green range of the electromagnetic spectrum. The spectral reflectance coefficient was used as a quantitative criterion for evaluating the reflective properties of snow and was used to recognize the type of snow.

One of the ways to measure the color of a natural object is to determine its color characteristics by using color coordinates (Table A1). The XY color coordinates are defined relative to the standard irradiance in the CIE 1931 (Commission Internationale de l'Eclairage) system, the spectral composition of which is close to that of solar energy [91]. The color coordinates CIE 1931 x, y are a conversion of the spectral data obtained from spectrometric measurements, as the whole spectral reflectance characteristic in the visible range is used [92]. The dominant wavelength and purity of color are characteristics in color analysis that are used in analyzing the spectral data from the spectrometric measurements obtained by the Sekonic C-800. The dominant wavelength is a color characteristic and a snow characteristic indicator, which is established by the color coordinates (x, y) of a standard source of electromagnetic radiation with the color coordinates (x, y) of the studied natural object, and in this case, it is snow [93]. This characteristic determines the boundaries within which snow can be defined as an object. The presence of snow is defined in the area from blue to blue-green color or in the spectral range (460–490) nm of the spectrometer used.

The mobile spectrometer data successfully verified the satellite data, detecting specific features that were not visible in the satellite data used. This is the case when the pixels are clear for other objects, and the values obtained are valid only for the object in question, which in this case is snow. The detailed characterization of the spectral reflectance could guide us regarding the presence of more water or ice in the snow patch. The physical condition and the color temperature provide us with a clear idea of the color of the object and the atmospheric conditions under which the studies were performed (dark or sunny and clear weather). The spectrometer provided important information that complemented and enriched the analysis of the satellite data and ensured the accuracy, reliability, and absence of subjective factors that were essential for performing reliable remote sensing.

The time required to conduct a single spectrometer measurement [94] is important, and, in this case, it was less than 10 s. The other types of field measurements were also performed within 1–2 min for each point in order to synchronize the field studies.

The mobile thermal camera gives visual information about temperature differences on surfaces in real time, and it is used indirectly to assess some surrounding features: places with ice, wet snow areas, warmer objects (individual infrastructure objects), and temperature imbalance. The temperature imbalance was observed in certain places where uneven temperature distribution was observed as some parts were significantly warmer or colder than others (Figures 5b, A4b and A5b).

3. Results

3.1. Test Site

Maps of the spatial distribution of the dB values of VH and VV polarizations in ascending and descending orbits of Sentinel 1 SAR images from 5 March 2024 and 11 March 2024 of the test site are shown in Figures 6 and 7, Table 2.

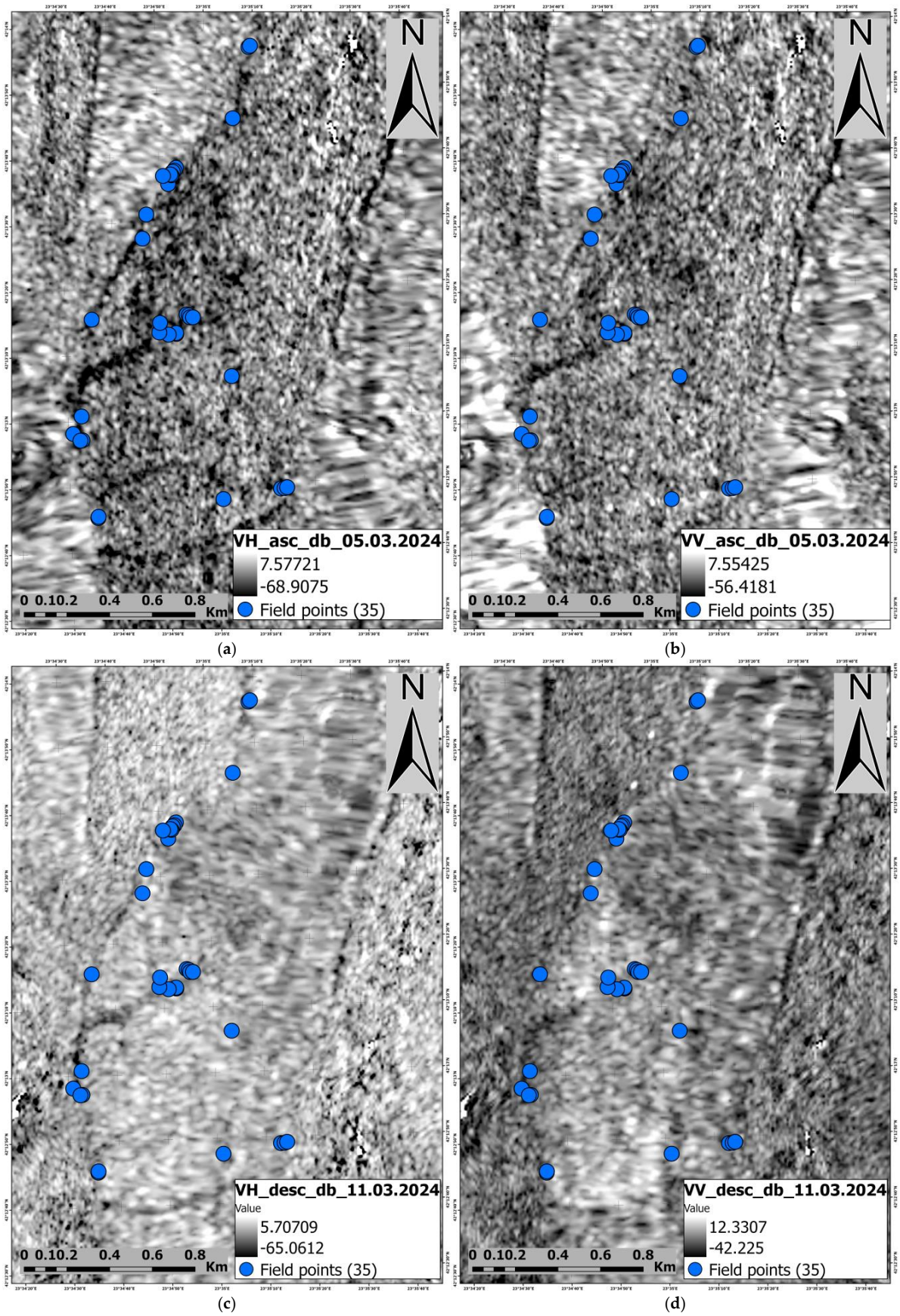

Figure 6. SAR images of the test site in VH (**a**) and VV (**b**) polarization in ascending orbit from 5 March 2024 and in VH (**c**) and VV (**d**) polarization in descending orbit from 11 March 2024 (dB values).

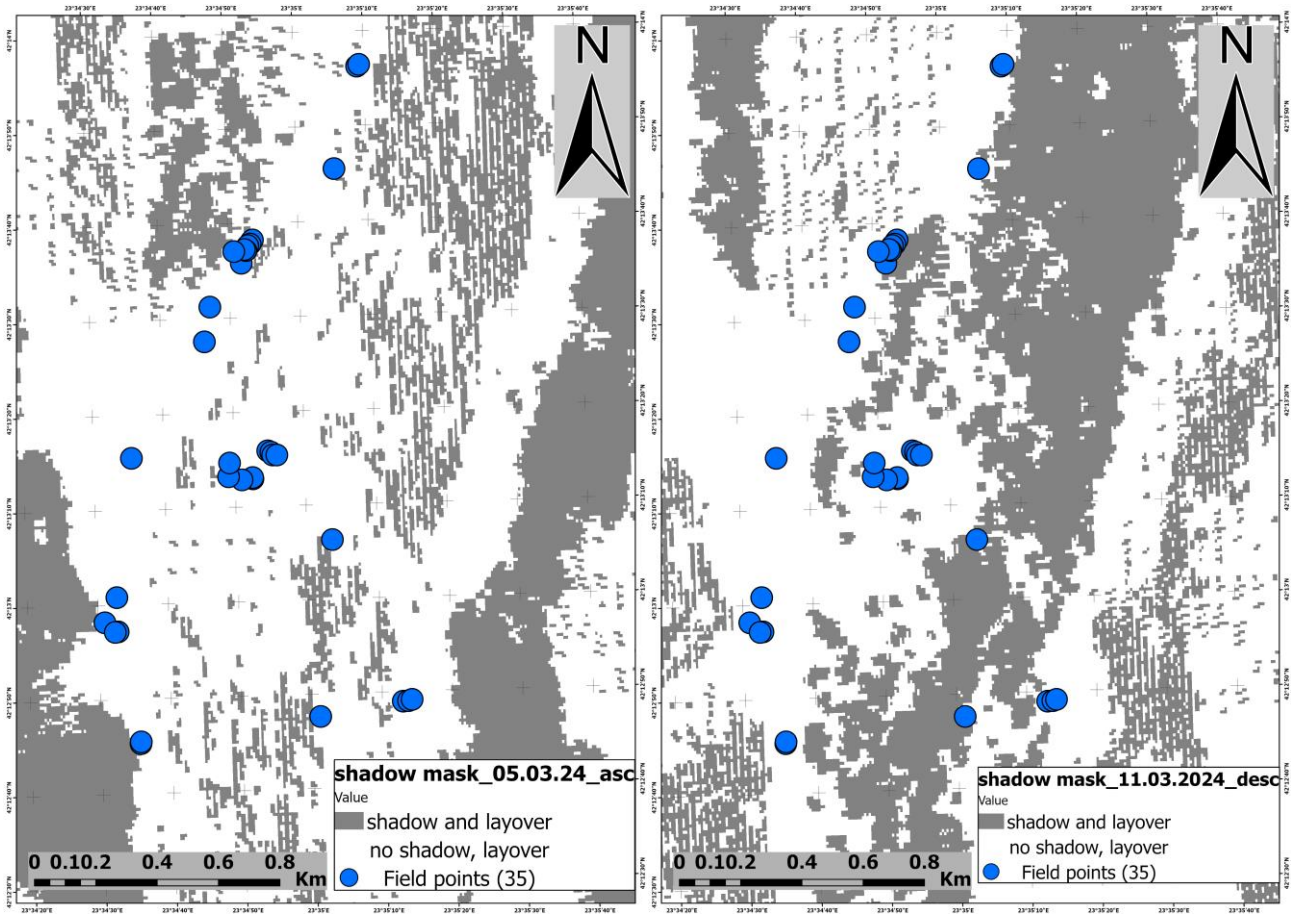

Figure 7. Shadow mask (**a**) 5 March 2024 ascending orbit, (**b**) 11 March 2024 descending orbit.

Table 2. Pixel values from VH and VV polarizations in ascending and descending orbits in dB (Sentinel 1 SAR images—5 March 2024 and 11 March 2024) and NDSII-2 (PlanetScope image—4 March 2024), Color Temperature (CCT) test site.

ID	Points	Snow Type	Asc VV	Asc VH	Desc VV	Desc VH	PlanetScope PSB.SD NDSII2	Color Temperature (CCT), [K]
1	3	Wet snow	−11.72	−18.2	−7.99	−20.27	−0.119	5794
2	4	Wet snow	−10.81	−18.37	−9.14	−22.33	−0.013	5837
3	44	Wet snow	−10.14	−19.52	−6.5	−17.56	−0.003	5770
4	45	Wet snow	−12.39	−21.6	−6.1	−15.59	0.023	5790
5	46	Wet snow	−10.4	−19.64	−6.57	−18.27	0.025	5794
6	15	Hard-packed	−9.74	−15.15	−3.86	−13.34	−0.002	5990
7	16	Hard-packed	−11.14	−15.58	−2.7	−12.76	0.010	5990
8	24	Hard-packed	−8.46	−16.31	−11.16	−14.88	−0.010	5910
9	25	Hard-packed	−11.88	−15.38	−10.64	−15.97	−0.002	5839
10	27	Hard-packed	−12.98	−22.89	−14.97	−22.01	0.000	5839
11	28	Hard-packed	−9.83	−18.43	−15.71	−21.31	−0.003	5839
12	39	Hard-packed	−14.73	−19.84	−5.97	−19.69	−0.030	6282
13	50	Hard-packed	−7.93	−16.51	−9.27	−13.32	−0.010	5817

Table 2. *Cont.*

ID	Points	Snow Type	Asc VV	Asc VH	Desc VV	Desc VH	PlanetScope PSB.SD NDSII2	Color Temperature (CCT), [K]
14	58	Hard-packed	−9.99	−17.17	−7.6	−16.27	−0.015	6099
15	61	Hard-packed	−12.87	−15.46	−5.44	−19.29	−0.022	6099
16	1	Powder snow	−8.9	−17.42	−9.54	−18.12	−0,029	6011
17	5	Powder snow	−12.29	−21.41	−13.09	−13.89	−0.032	6137
18	6	Powder snow	−9.38	−12.52	−10.27	−19.03	−0.09	5928
19	8	Powder snow	−9.7	−14.31	−5.75	−13.93	−0.034	5928
20	9	Powder snow	−10.42	−16.09	−5	−14.14	−0.012	5847
21	10	Powder snow	−10.72	−16.84	−5.07	−14.09	−0.057	5820
22	14	Powder snow	−12.61	−16.54	−2.61	−14.29	−0.040	6177
23	17	Powder snow	−6.6	−14.95	−2.78	−17.32	−0.082	5841
24	29	Powder snow	−7.61	−16.71	−13.7	−19.1	−0.011	5933
25	30	Powder snow	−9.61	−15.9	−8.87	−13.24	−0.014	5933
26	31	Powder snow	−16.05	−24.44	−14.57	−17.71	−0.020	6207
27	33	Powder snow	−10.58	−17.95	−11.93	−20.27	−0.030	6137
28	38	Powder snow	−12.24	−18.8	−12.75	−23.59	−0.030	6045
29	42	Powder snow	−11.86	−14.95	−4.83	−12.54	−0.010	6001
30	47	Powder snow	−7.64	−20.11	−8.62	−16.26	−0.034	6001
31	48	Powder snow	−4.22	−20.59	−9.83	−13.44	−0.034	6001
32	52	Powder snow	−9.41	−13.55	−7.11	−12.18	−0.038	6011
33	60	Powder snow	−12.87	−15.46	−5.44	−19.29	−0.022	6120
34	63	Powder snow	−8.92	−15.22	−11.88	−14.21	−0.068	6258
35	64	Powder snow	−8.15	−14.72	−11.16	−13.87	−0.003	6258

In Figure 6a, Table 2 in VH polarization ascending orbit, Point 1 and Point 5 (powder snow) have a value of −17.42 dB and −21.41, Point 3 and 46 (Wet snow)—−18.20 dB and −19.64 dB, and Point 50 and 61 (hard-packed snow)—−16.51 dB and −15.46 dB. Of the selected profile points with the greatest minimum, those from powder snow have the minimum dB value of all selected field points—−21.41 dB (Table 2, Column 5, Table 3), and for all points it is −24.44 dB.

Table 3. Results from VH and VV polarizations in ascending orbit in dB (Sentinel 1 SAR images—5 March 2024).

Asc VV	Wet Snow	Hard-Packed Snow	Powder Snow
min	–	–	V
max	–	–	V
asc VH	**Wet snow**	**Hard-packed snow**	**Powder snow**
min	–	–	V
max	–	–	V

In VV polarization in ascending orbit (Figure 6b) values for points 1, 5, 3, 46, 50, and 61 are –8.9 dB; −12.29 dB; −11.72 dB; −10.4 dB; −7.93 dB; and −12.87 dB, respectively, where Point 5 (powder snow) has the minimum value close to that of hard-packed snow (Table 2, Column 4). From the measured profiles of all points, the minimum value is −16.05 dB for powder snow, and the maximum is again for powder snow with a value of −4.22 dB (Table 3).

In Figure 6c, VH polarization descending orbit values for points 1, 5, 3, 46, 50, and 61 are −18.12 dB; −13.89 dB; −20.27 dB; −18.27 dB; −13.32 dB; and −19.29 dB, respectively, where Point 3 (wet snow) has the minimum value of all selected field points (Table 2, Column 7). From all measured points, the minimum is −23.99 for powder snow, and the maximum is −12.18 dB, which is again for powder snow (Table 4).

Table 4. Results from VH and VV polarizations in descending orbit in dB (Sentinel 1 SAR images—11 March 2024).

Desc VV	**Wet Snow**	**Hard-Packed Snow**	**Powder Snow**
min	–	–	V
max	–	V	–
desc VH	**Wet snow**	**Hard-packed snow**	**Powder snow**
min	–	–	V
max	–	–	V

In VV polarization descending orbit (Figure 6d) values for points 1, 5, 3, 46, 50, and 61 are −9.54 dB; −13.09 dB; −7.99 dB; −6.57 dB; −9.27 dB; and −5.44, respectively, where Point 5 (powder snow) has the minimum value of all selected field points (Table 2, Column 6). The maximum for all points is −2.61 dB and is for powder snow, while the minimum is for hard-packed snow, which has a value of −15.71 dB (Table 4).

The 35 field data points selected in the present study do not fall into radar layover, foreshortening, and shadows, as the rest of the terrain-collected field data points (more than 70) were excluded (Figure 7). All radar layover, foreshortening, and shadows are merged and shaded in gray in Figure 7.

Maps of the spatial distribution of powder, hard-packed, and wet snow according to the RGB composite of PlanetScope VHR image and NDSII2 values, calculated from 4 March 2024, are shown in Figure 8a,b, serving as alternative validation methods. Pixel values from VH and VV polarizations in ascending and descending orbits in dB of Sentinel 1 SAR images (5 March 2024 and 11 March 2024) and NDSII2 of PlanetScope image (4 March 2024) of the collected data field points are shown in Table 2. For the calculation of NDSII-2, Band 4 and Band 8 of the PlanetScope image were used (Table 1).

3.2. Validation Using In Situ Data

The following values have been obtained in a visible range of the electromagnetic spectrum by means of the Sekonic C-800 spectrometer and validated image data (Figures 5, A4 and A5). The spectral reflectance gradually increases from 380 to 420 nm, where the relative value reaches about 0.8 at 420 nm. The range of blue and blue-green shows the highest values at 460 nm for the test site, with characteristic values from 0.99 to 1. At 480 nm, the value is one, and for 540 nm, it ranges from 0.9 to 0.94. The spectral reflection values around ~760 nm are the lowest and range from 0.48 to 0.58. Regarding the obtained values for the color parameters, the following conclusions were drawn:

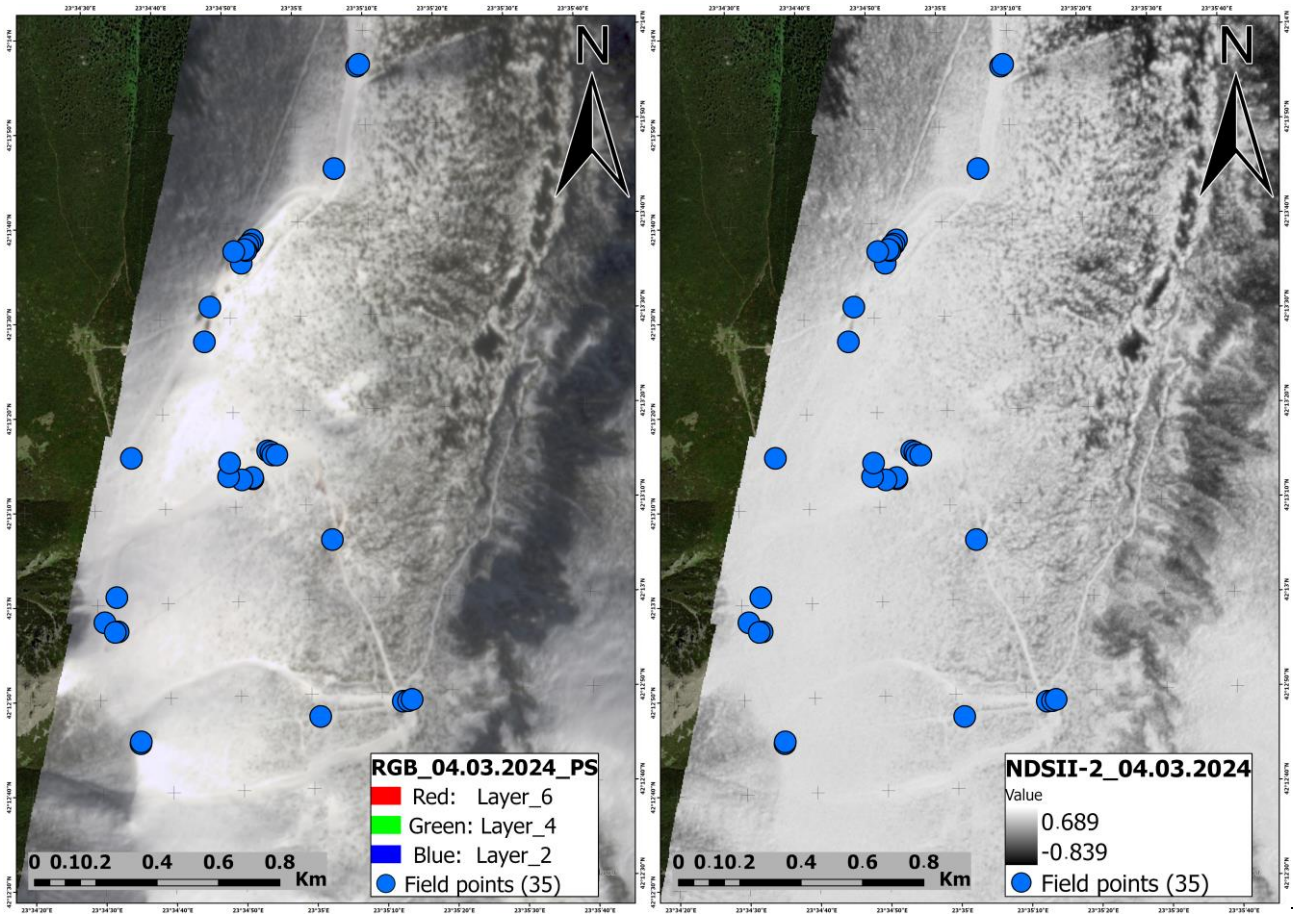

(**a**) (**b**)

Figure 8. PlanetScope image from 4 March 2024—RGB composite (**a**) and NDSII2 values (**b**) of the test site ("Image © 2024 Planet Labs PBC").

An average Correlated Color Temperature (CCT) of 5975.8 K for the test area was calculated. These are relatively high values and ensure that they were measured in natural light, since the color temperature of sunlight at noon is above 5500 K. Values from 5500 to 6500 K are so-called "cold colors", which verifies the presence of a white or cold color characteristic of the snow in the test area (Figure 4).

Also, the CRI values are high. A CRI equal to 100 Ra is assumed to be daylight (sunlight), and in this particular case, it is equal to 99, or an extremely high value. At this value of light, the colors of the observed objects are perceived most naturally. The same applies to the other values of R1 to R15, which, for the object in the case of snow, are on average 99. These values are also observed for the other objects. CRI measures all color ranges from R1 to R15, but the RA value measures only the blue-green areas of the light fixture or sunlight, R1 to R8, at that Ra point = 99. The most difficult color to reproduce is red (R = 9), and in this particular example, it has the lowest values of R9 = 97.4 [95] (Figures A2 and A3, Table A1). For all profiles, the R-9 values are above 95%, and the Ra values range from 97.6 to 99.4, which is a significantly high percentage. The evidence of accuracy from measurements made using ANSI/IES TM-30 standards is undeniable. The values of all profiles have similar data around Rf-99 and Rg-100 (Figure A3, Table A1).

The results of the minimum and maximum values measured by the thermal camera are negative and positive. This is also due to the fact that the research was carried out in the month of March and in warmer and sunnier weather, despite the high altitude of the test site. Only individual infrastructure objects (elevator facilities, fences, etc.) have

measured positive temperatures, and in this type of research, they are measured in degrees. To confirm the data from the thermal camera as a location, photos are attached for some of the objects. The ski slopes have lower temperatures than the places outside them, which is due to the hard-packed snow, which, in some places, turns into ice (Figure A5b).

4. Discussion

The minimum backscatter dB values of SAR imagery usually correspond to snow, ice, and water areas due to the nonregistration of the active signal of the SAR antenna, reflected from the surface to the sensor [78,96]. In the present study, only snow in different state phases was studied. The minimum backscatter dB values were generally registered for P31 (powder snow) in the test site, reaching up to −24.41 dB in VH polarization in ascending orbit (Table 3). Similarly, lower values than −23.50 dB were registered for P38 (powder snow) in the test site in VH polarization, descending orbit (Table 4). The lowest values obtained for the hard-packed snow and the powder snow are related to the backscatter characteristics of these surfaces in radar imagery (Figure 9).

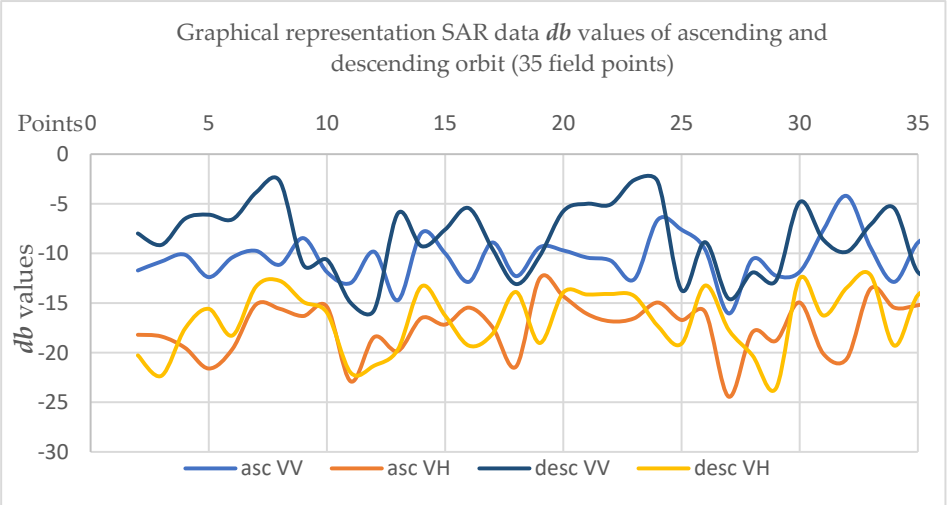

Figure 9. Graphical representation of SAR data in db values of ascending and descending orbit (35 field points), Sentinel 1 SAR, ESA.

All these statements are visualized in Figure 9 for a clearer idea of the summary for each polarization. In order not to overload the graph, the identification numbers described in Table 2 have been used for each point. The points start from wet snow (1–5), hard-packed snow (6–15), and end with powder snow (16–35) for each polarization type and orbit.

Due to its fine, fluffy texture, which scatters the radar signal away from the sensor, the powder snow is characterized by very low backscatter values. Similar backscatter features have the smooth surfaces of ice and hard-packed snow. The points falling into mixed pixels of Sentinel-1 have higher backscatter values due to the vegetation on them. However, the results obtained from the field measurements for these points clearly show the typical snow spectrometric curve (Figures 5a and A5a). These results are consistent with the findings of [37–39] that the signal obtained in cross-polarization carries more specific information about the surface features and could be successfully used for distinguishing snow covers from other surfaces.

Wet snow has lower reflection properties and appears darker in the optical spectrum, giving intermediate values in the applied optical indices, and is therefore harder to detect. These results are confirmed by the reflection curve of wet snow, characterized by high values of 380–460 nm and the lowest values of ~760 nm due to the high presence of liquid water in the snow (Figure A4a).

Considering the influence of the acquisition parameters, the dB backscatter values in the VV polarization mode for the same point locations or the same states of snow reported higher dB values than the values in the VH polarization mode. Generally, the cross-polarized data shows a lower backscatter value than co-polarized data, which can also be seen in other studies [97].

The analysis of optical satellite data shows that the maximum values of optical data indices correspond generally to the minimum values of SAR backscatter data for objects consisting of water and moisture (Figures 9 and 10).

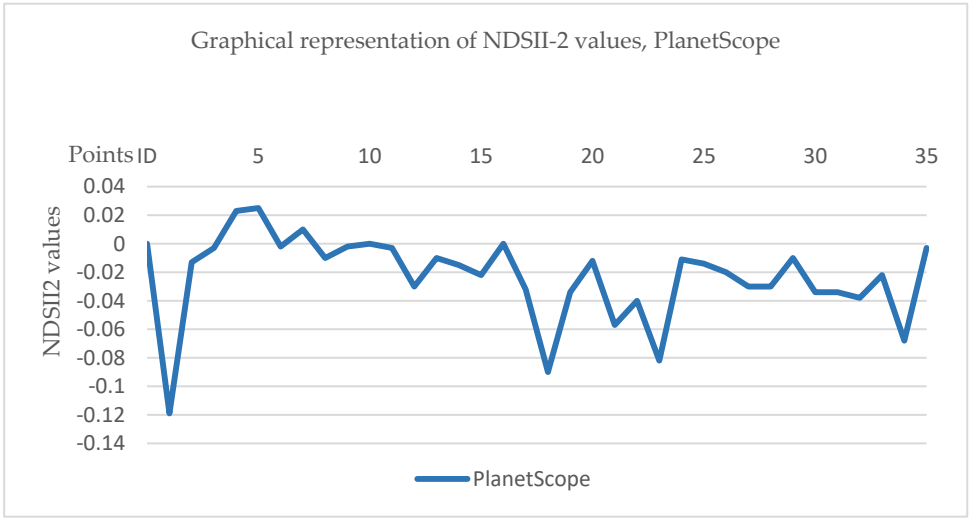

Figure 10. Graphical representation of the NDSII2 values, PlanetScope, 4 March 2024.

The thermal camera measurements recorded higher surface temperatures as the measurements were performed in the early spring (March), 4 March 2024 and coincide with the date of PlanetScope satellite data. The higher temperatures determined the onset of melting in the area and the higher presence of liquid water in the snowpack. The thermal imaging data were used only as a verifier for the studied area and snow conditions, since a typical characteristic of the spectral emissivity of snow is observed at wavelengths λ = 11–13 µm. This study does not aim to perform a detailed analysis of the thermal imaging data because there is enough freely available satellite data for Land Surface Temperature (LST).

The maximum value for SAR data from P4 is—0.01, and, compared with all four sets of SAR values, it has the highest correspondence with the minimum backscatter dB value of VH polarization in descending orbit—−22.33 dB due to the presence of liquid water in the snowpack. The presence of liquid water in the snowpack at this point was also confirmed by the character of the spectrometric curve, where a clear drop of ~760 nm was observed. The presence of liquid water is also indicated by the spectral signature of P5. The presence of liquid water in it is confirmed by both types of field measurements (thermal and spectrometric) and also by the lower dB values ranging from ~−12 to ~−22 dB. Similar dB values in VV polarization, descending orbit, were obtained from [98] identification of wet snow during seasonal snow phase changes (Figure 9).

Dry snow (hard-packed snow) and ice have higher reflection properties and appear brighter in the optical spectrum and thus provide the highest values of the applied optical indices, while in the microwave spectrum, there is a clear distinction between the results obtained for these two objects. In this case, the values of VH polarization in descending orbit and the VV polarization in ascending orbit provide the most accurate information for distinguishing hard-packed snow and powder snow, where the ice reflectance curve has lower values in the blue range of the electromagnetic spectrum than those in the dry

snow reflectance curve. Ice has higher values in the green range than those of powder snow (Figures 5 and A5, Table 2).

According to the results obtained from the SAR datasets used in the study, it could be summarized that for wet snow detection, the VH polarization dB values in the descending orbit provide useful information. The powder snow was properly detected by the VH and VV polarizations in ascending orbit and by VV polarization in descending orbit. The heterogeneous areas consisting of snow and vegetation were most accurately detected by the VV polarization in descending orbit.

The main advantage of the present study is that the slope aspects, the effect of the position of the sensing instrument (especially of SAR), and the behavior of the different polarization modes in the case of radar shadows were taken into account. The main disadvantage is that SAR data with different wavelengths (S, L, and P bands) and higher spatial resolutions are not included, so that the analysis can be richer and more in-depth.

The selected points from the field measurements are in locations not shaded by adjacent slopes in order to effectively use available SAR data, and the data were validated with data from all key parts of the electromagnetic spectrum for snow such as the visible range (from spectrometer and optical data from PlanetScope) and the thermal range of 8–14 μm.

5. Conclusions

In the present study, satellite data and snow cover monitoring methods were compared in the high mountain belt of Bulgaria. The performance of spectral indices as SAR indices based on cross-polarized VH data and co-polarized VV data in ascending and descending orbits was analyzed. The performance of the studied indices was assessed using in situ data from a field spectrometer and thermal camera. The results outlined some specifics of the studied data and methods that could be helpful for further studies of snow cover. By the applied integrative method, the research is focused on utilizing the valuable information from each remote sensing instrument used in the study, which can be integrated and updated for future studies related to snow monitoring.

Generally, the study confirms the findings that cross-polarized SAR data could be successfully used for distinguishing surface features of the snow, and co-polarized images are suitable for studies of the physical properties of the snow. In the presented research, VH polarized data in ascending orbit distinguished most accurately the fresh accumulated snow cover, and VH polarization in descending orbit was the most suitable for distinguishing ice and hard-packed snow. From the SAR datasets, VV polarization in descending orbit provided the most accurate information for the detection of hard-packed snow and wet snow [99]. In both types of polarization, VV and VH for asc and desc orbit, powder snow is distinguished in the minimum (Tables 2–4). The results obtained from the SAR data in this study can only be interpreted uniformly for the three types of snow that have been studied at this stage.

All curves of mobile spectrometer data have an even distribution of light in the blue, green, and red parts of the spectrum, since they are all from snow. The selected points (35 points) on which a spectral profile was made have a color temperature from 5794 K to 6282 K, which indicates cool light, closer to daylight (Figure 3). This proves that the spectral characteristics were made entirely in daylight, which is also proven by the operator's in situ data. In the red part of the visible electromagnetic spectrum, all curves are almost similar, with dips only between 730 and 760 nm, which confirms that this is snow. Drops in intensity were observed in different parts of the spectrum, which indicate a weaker ability of these light sources to accurately reproduce some colors (especially in the red and violet parts).

It is difficult to distinguish the three types of snow using this type of spectrometer based on the spectral curve alone, but when individual parameters are analyzed, the difference can be noticed. It is most obvious in the color temperature, which is highest for powder snow above 6000 K, or an average for this study of 6029 K, lower for hard-packed snow around 5970 K, and lowest for wet snow (Figure 11). The color coordinates confirmed that the object was snow, and parameters such as Rf, Rg, and Ra confirmed the conclusions about the colors of the observation objects.

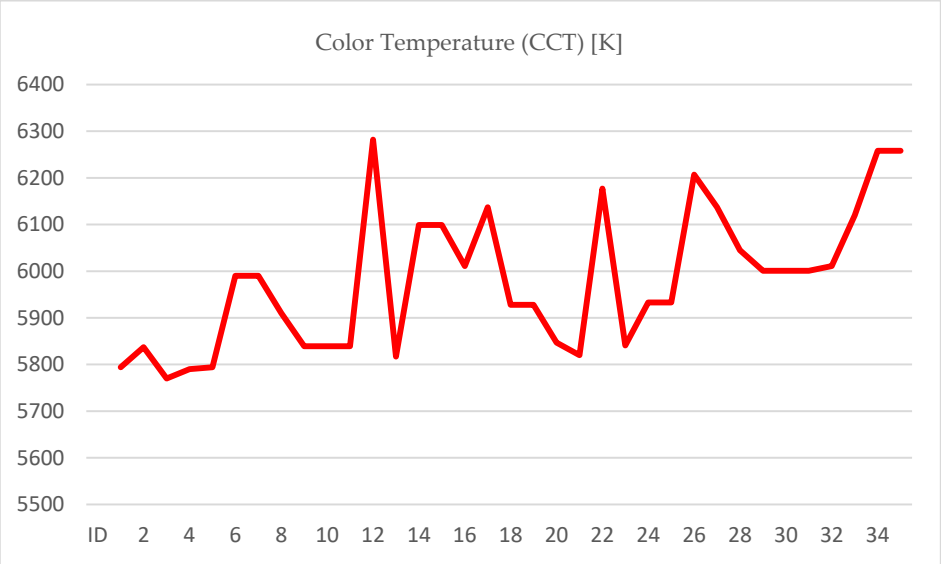

Figure 11. Graphical representation of the relationship between Correlated Color Temperature (CCT) [K], 4 March 2024.

Spectrometers can detect small changes in spectral characteristics that cannot be seen by satellite images of lower spatial resolution. This is useful for the early detection of stress in different objects, including the dynamics of snow and its different states. Field spectrometer data provide important information that complements and enriches satellite data [76]. The color rendering index (CRI) and the data for the 15 colors (from R1 to R15) show high values. The general CRI Ra values are 99 out of a maximum of 100 for the three types of snow, which means a value close to the real colors of the objects under study (Table A1), which was also confirmed by the operator's field photos. The values presented in profile 1 for color rendering are no exception to the rest, as can be seen from the values in Table A1 for the three types of snow.

All parameters studied by the spectrometer can supplement and upgrade the information not only for the three types of snow but also for any other object, as long as we know the spectral curve of the studied object well enough. Information from spectrometric data does not replace the use of satellite data (optical or radar) since it is a question of different spatial resolutions. This information helps the integrated approach, as it enriches the momentary information, which may not coincide with the temporal and spatial resolution of the satellites.

Supplementing field data with thermal imaging camera measurements provides multiple benefits. The use of a ground-based thermal camera can be useful for showing high temperatures in late winter and early spring. The data show positive values for this high altitude in most images.

These studies can be used to validate satellite thermal images and ensure that the temperatures measured by the satellites match the actual temperatures on the Earth's surface [100]. Ground-based thermal cameras can provide detailed information on small-scale

temperature changes, which is particularly useful in areas where microclimatic conditions can vary greatly, such as mountain areas. Ground-based thermal cameras can identify thermal anomalies that may not be visible in lower-resolution satellite imagery, which can be of great benefit for prevention purposes, and their data can be used as an indicator of the presence of avalanches.

In conclusion, the obtained data and results are sufficient for analysis based on SAR and in situ data in the high mountain belt and can be applied in snow cover monitoring methodologies.

Author Contributions: Conceptualization, A.S., T.S. and D.A.; methodology, T.S., A.S. and D.A.; software, A.S. validation, T.S.; formal analysis, A.S., T.S. and D.A.; investigation, A.S. and D.A.; resources, A.S.; data curation, A.S.; writing—original draft preparation, T.S., A.S. and D.A.; writing—review and editing, A.S., D.A. and T.S.; visualization, A.S., T.S. and D.A.; supervision, A.S.; project administration, A.S.; funding acquisition, A.S. All authors have read and agreed to the published version of the manuscript.

Funding: This study is a part of project "Monitoring of the seasonal dynamics and stability of the snow cover in the mountain range of the Republic of Bulgaria for a period of 10 years (2014–2024) based on Remote Sensing" financed by the National Science Fund of Ministry of Education and Science of Republic of Bulgaria under contract № KP-06-M64/1.

Data Availability Statement: The original contributions presented in this study are included in the article. Further inquiries can be directed to the corresponding author.

Conflicts of Interest: The authors declare no conflicts of interest.

Appendix A

Table A1. Spectrometer data for the selected in situ profiles 1, 5, 46, 50, 61 for the test site.

Spectral Parameters	Value Point 1 Powder Snow	Value Point 5 Powder Snow	Value Point 46 Wet Snow	Value Point 50 Hard-Packed	Value Point 61 Hard-Packed
CCT [K]	6011	6137	5794	5817	6099
CRI, Ra	99	98.9	99.4	99.2	99.0
CRI R1	98.7	98.5	99.5	99.0	98.7
CRI R2	98.9	98.8	99.3	99.0	98.9
CRI R3	99.6	99.7	99.5	99.5	99.7
CRI R4	98.8	98.6	99.5	98.9	98.7
CRI R5	98.6	98.5	99.4	98.8	98.6
CRI R6	98.7	98.6	99.2	99.5	98.7
CRI R7	99.7	99.8	99.4	99.8	99.8
CRI R8	99.3	99.0	99.5	99.1	99.2
CRI R9	97.4	96.6	99.0	99.0	97.2
CRI R10	97.9	97.8	98.8	98.2	97.9
CRI R11	98.4	98.2	99.3	98.7	98.3
CRI R12	97.1	97.0	97.9	97.2	97.1
CRI R13	98.6	98.4	99.2	98.8	98.5
CRI R14	99.8	99.8	99.8	99.7	99.8
CRI R15	98.6	98.3	99.5	99.0	98.5
CIE1931 x	0.3220	0.3194	0.3260	0.3255	0.3201
CIE1931 y	0.3335	0.3319	0.3389	0.3379	0.3327
Hue	29 deg	28 deg	39 deg	37 deg	30 deg
Saturation	5%	4%	9%	9%	4%
TM 30-18	Rf = 99	Rf = 99	Rf = 99	Rf = 99	Rf = 99
TM 30-18	Rg = 100	Rg = 101	Rg = 100	Rg = 100	Rg = 101
TM 30-18	Ra = 99.0	Ra = 98.9	Ra = 99.4	Ra = 99.2	Ra = 99.0

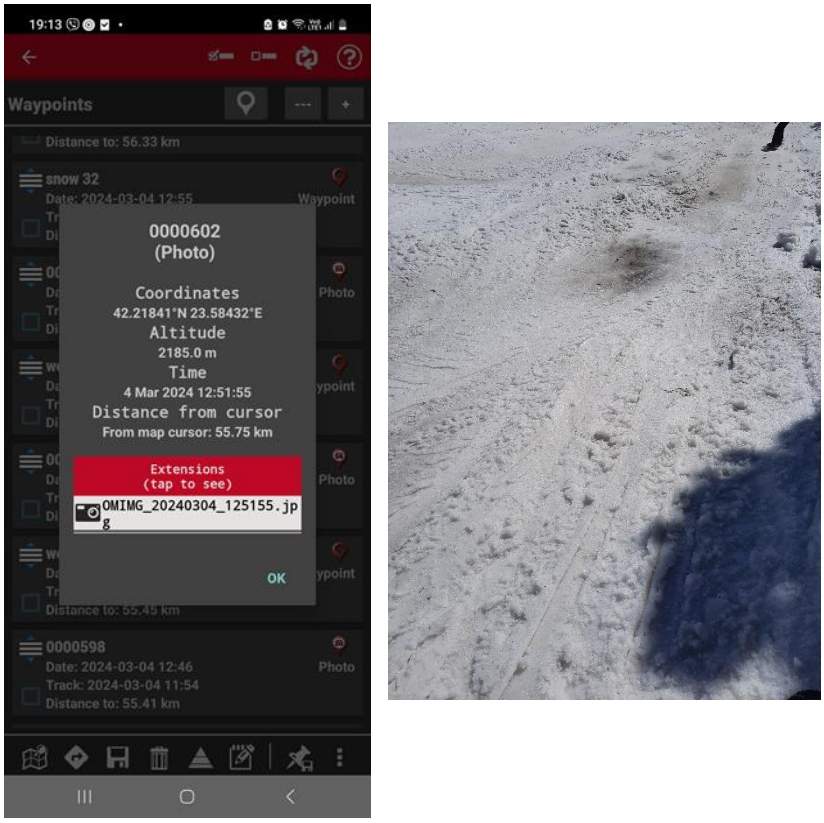

Figure A1. Example of a wet snow profile with GPS coordinates generated by OruxMaps and images.

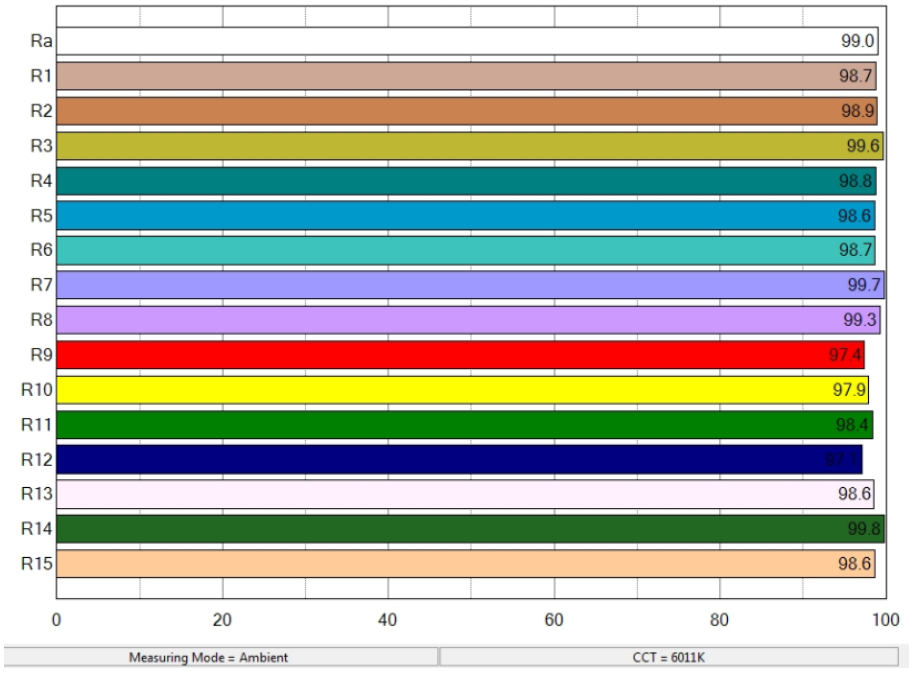

Figure A2. Color rendering index (CRI), R1–R15, profile 1 of the test site, shows high values above 95 for all colors. The general CRI Ra value is 99 out of a maximum of 100, which means a high value, close to the real colors of the object of 100 (Table A1).

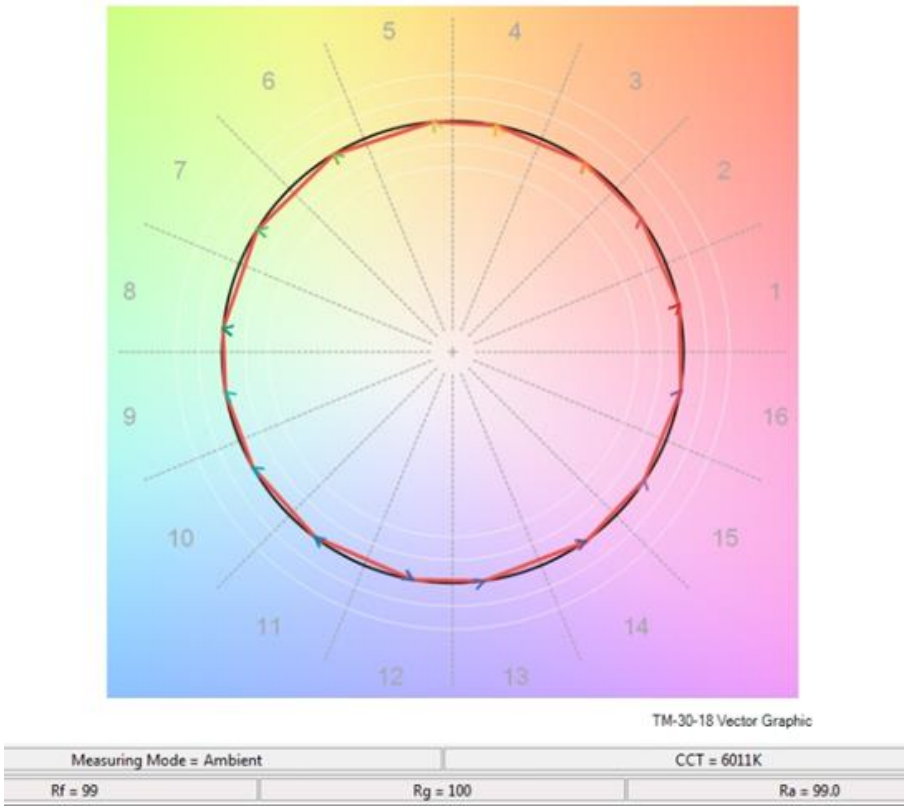

Figure A3. A lighting color rendition standard TM-30-18 report: TM-30 metrics and Color Vector Diagram, profile 1 of the test site (Table A1). The values for Rf are 99 out of a maximum of 100, Rg is 100 and falls within the baseline values, Ra is 99 out of 100, meaning the values are close to the real colors. The profile is presented with the perfect values from the internationally accepted sets of guidelines for displaying the performance of flowers.

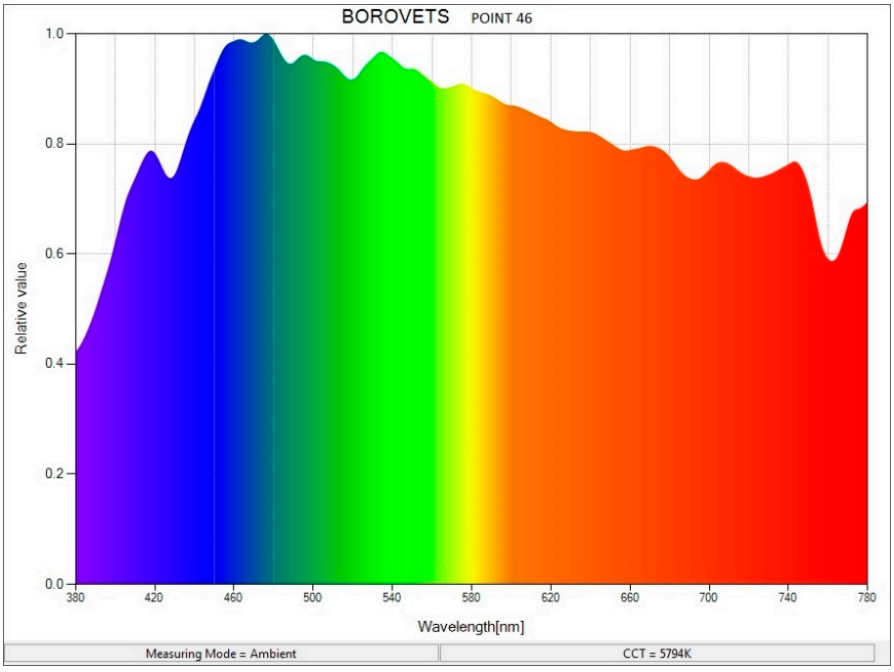

(**a**)

Figure A4. *Cont.*

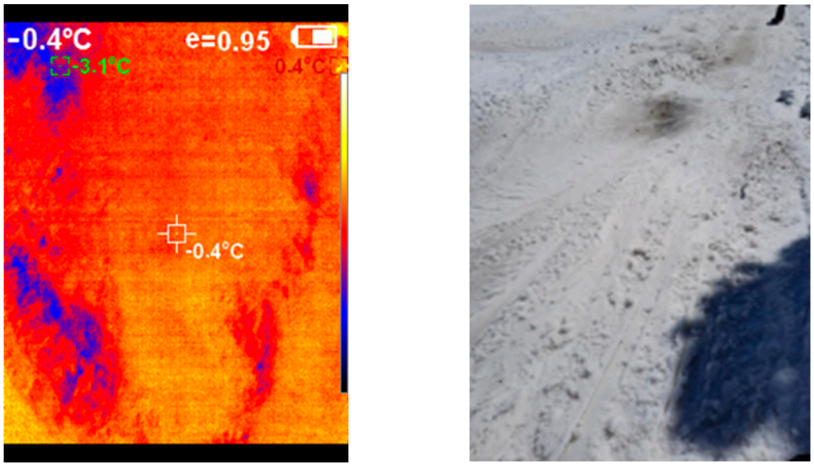

(**b**) (**c**)

Figure A4. Wet snow, point 46. (**a**) Spectral reflectance curve of the wet snow, Sekonic C-800 mobile spectrometer. (**b**) Thermal image of the area of interest around the survey point, time 12:12:01, HT-19 thermal camera. Photo of the wet snow in the area of interest around the survey point. (**c**) Photo of the wet snow in the area of interest around the survey point.

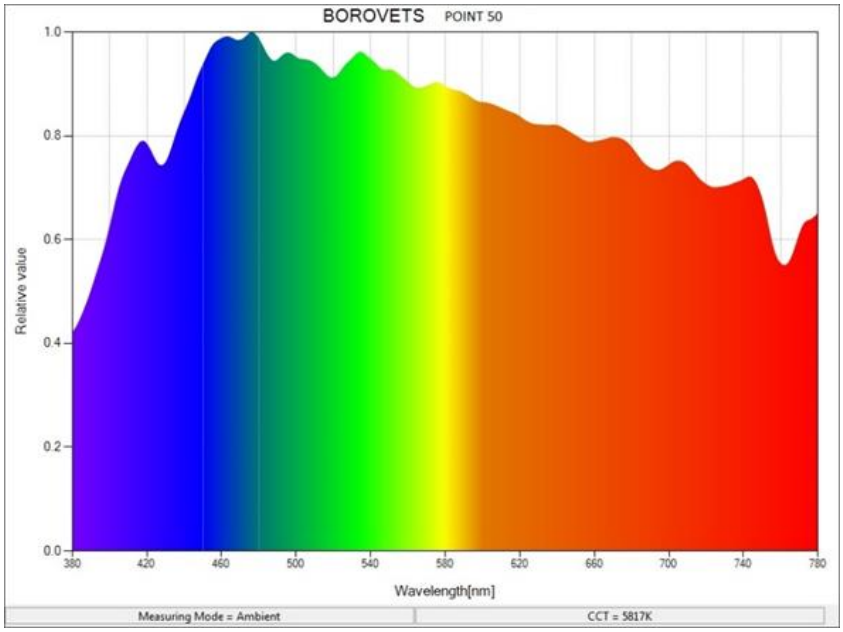

(**a**)

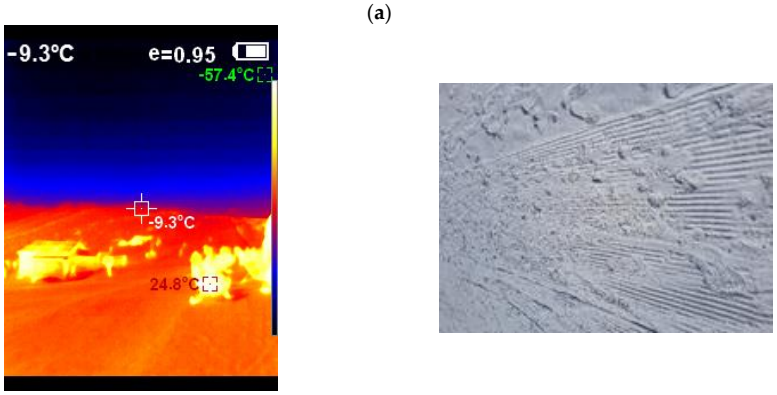

(**b**) (**c**)

Figure A5. Hard-packed snow, point 50. (**a**) Spectral reflectance curve of the hard-packed snow, Sekonic C-800 mobile spectrometer. (**b**) Thermal camera image, t121228Thermal image of the area of interest around the survey point, time 12:12:28, HT-19 thermal camera. (**c**) Photo of the hard-packed snow of the area of interest around the survey point.

References

1. Viviroli, D.; Weingartner, R. The hydrological significance of mountains: From regional to global scale. *Hydrol. Earth Syst. Sci.* **2004**, *8*, 1017–1030. [CrossRef]
2. Fernandes, R.A.; Zhou, F.; Song, H. *Evaluation of Multiple Datasets for Producing Snow-Cover Indicators for Canada*; Geomatics Canada: Ottawa, ON, Canada, 2017.
3. Dixit, A.; Goswami, A.; Jain, S. Development and Evaluation of a New "Snow Water Index (SWI)" for Accurate Snow Cover Delineation. *Remote Sens.* **2019**, *11*, 2774. [CrossRef]
4. Gupta, R.P.; Haritashya, U.K.; Singh, P. Mapping dry/wet snow cover in the Indian Himalayas using IRS multispectral im-agery. *Remote Sens. Environ.* **2005**, *97*, 458–469. [CrossRef]
5. Shimamura, Y.; Izumi, T.; Matsumaya, H. Evaluation of a useful method to identify snow-covered areas under vegetation–comparisons among a newly proposed snow index, normalized di erence snow index and visible reflectance. *Int. J. Remote Sens.* **2006**, *27*, 4867–4884. [CrossRef]
6. Sibandze, P.; Mhangara, P.; Odindi, J.; Kganyago, M. A comparison of Normalised Di erence Snow Index (NDSI) and Nor-malised Di erence Principal Component Snow Index (NDPCSI) techniques in distinguishing snow from related land cover types. *S. Afr. J. Geomat.* **2014**, *3*, 197–209. [CrossRef]
7. Valovcin, F.R. *Snow/Cloud Discrimination*; AFGL-TR-76-0174, ADA 032385; Air Force Geophysics Laboratory Hanscom AFB Mass: Bedford, MA, USA, 1976.
8. Valovcin, F.R. *Spectral Radiance of Snow and Clouds in the Near Infrared Spectral Region*; AFGL-TR-78-0289, ADA 063761; Air Force Geophysics Laboratory Hanscom AFB Mass: Bedford, MA, USA, 1978.
9. Kyle, H.L.; Curran, R.J.; Barnes, W.L.; Escoe, D. A cloud Physics Radiometer. In Proceedings of the Third Conference on Atmospheric Radiation, American Meteorological Society, Davis, CA, USA, 28–30 June 1978; p. 107.
10. Rees, W.G. *Remote Sensing of Snow and Ice*; CRC Press: Boca Raton, FL, USA, 2006; pp. 137–156.
11. Thakur, P.K.; Garg, R.D.; Aggarwal, S.P.; Garg, P.K.; Shi, J. Snow density retrieval using SAR data: Algorithm validation and applications in part of North Western Himalaya. *Cryosphere Discuss.* **2013**, *7*, 1927–1960. [CrossRef]
12. Rango, A.; Salomonson, V.V.; Foster, J.L. Employment of satellite snow cover observations for Improving Seasonal Runoff Estimates. In *Operational Applications of Satellite Snow Cover Observations*; NASA-SP-391; NASA: Washington, DC, USA, 1975; pp. 157–174.
13. Dhanju, M.S. Studies of Himalayan snow cover area from satellites. Hydrological Applications of Remote Sensing and Remote Data Transmission. In Proceedings of the Hamburg Symposium, IAHS, Hamburg, Germany, 15–26 August 1983; Volume 145, pp. 401–409.
14. Dozier, J. Snow reflectance from Landsat-4 Thematic Mapper. *IEEE Trans. Geosci. Remote Sens.* **1984**, *22*, 323–328. [CrossRef]
15. Dozier, J. Spectral signature of Alpine snow cover from the Landsat Thematic Mapper. *Remote Sens. Environ.* **1989**, *28*, 9–22. [CrossRef]
16. Hall, D.K.; Riggs, G.A.; Salomonson, V.V. Development of methods for mapping global snow cover using moderate resolution imaging spectroradiometer data. *Remote Sens. Environ.* **1995**, *54*, 127–140. [CrossRef]
17. Dozier, J. Remote Sensing of the Alpine Snow Cover: A Review of Techniques and Accomplishments from the Visible Wavelengths Through the Microwave. In Proceedings of the International Conference on Snow 5 Hydrology the Integration of Physical, Chemical, and Biological Systems, Brownsville, VT, USA, 6–9 October 1998; 03755-1290, Special Report. US Army Cold Regions Research and Engineering Laboratory Hanover: New Hampshire, NH, USA, 1998; pp. 98–110.
18. Dozier, J.; Painter, H.T. Multispectral and hyperspectral remote sensing of alpine snow properties. *Annu. Rev. Earth Planet. Sci.* **2004**, *32*, 465–494. [CrossRef]
19. Braun, M.; Rau, F. Using a multi-year data archive of ERS-SAR imagery for monitoring snow line positions and ablation patters on the King George Island ice cap (Antarctica). *EARSeL eProc.* **2001**, *1*, 281–291.
20. Rau, F.; Braun, M.; Friedrich, M.; Weber, F.; Gobmann, H. Radar glacier zones and its boundaries as indicators of glacier mass balance and climatic variability. *EARSeL eProc.* **2001**, *1*, 317–327.
21. Storvold, R.; Malnes, E.; Larsen, Y.; Høgda, K.A.; Hamran, S.E.; Muller, K.; Langley, K.A. SAR Remote Sensing of Snow Parameters in Norwegian Areas—Current Status and Future Perspective. In Proceedings of the Progress in Electromagnetics Research Symposium, Cambridge, MA, USA, 26–29 March 2006; pp. 182–186.
22. Thakur, P.K.; Snehmani, P.V.H.; Aggarwal, S.P.; Jain, S.K. Snow Cover Mapping Using Multi-Sensor SAR Data for Parts of Western Himalayas. In Proceedings of the International Symposium on Snow and Avalanches (ISSA), at Snow and Avalanche Establishment (SASE), Manali, India, 6–10 April 2009.
23. Venkataraman, G.; Singh, G.; Kumar, V. Snow Cover Area Monitoring Using Multitemporal TerraSARX Data. In Proceedings of the Third TerraSAR-X Science Team Meeting, DLR, Hamburg, Germany, 25–26 November 2008.
24. Wang, L.; Toose, P.; Brown, R.; Derksen, C. Frequency and distribution of winter melt events from passive microwave satellite data in the pan-Arctic, 1988–2013. *Cryosphere* **2016**, *10*, 2589–2602. [CrossRef]

25. Grenfell, T.C.; Putkonen, J. A method for the detection of the severe rain-on-snow event on Banks Island, October 2003, using passive microwave remote sensing. *Water Resour. Res.* **2008**, *44*, 1–9. [CrossRef]
26. Dolant, C.; Langlois, A.; Montpetit, B.; Brucker, L.; Roy, A.; Royer, A. Development of a rain-on-snow detection algorithm using passive microwave radiometry. *Hydrol. Process.* **2016**, *30*, 3184–3196. [CrossRef]
27. Langlois, A.; Johnson, C.A.; Montpetit, B.; Royer, A.; Blukacz-Richards, E.A.; Neave, E.; Dolant, C.; Roy, A.; Arhonditsis, G.; Kim, D.K.; et al. Detection of rain-on-snow (ROS) events and ice layer formation using passive microwave radiometry: A context for Peary caribou habitat in the Canadian Arctic. *Remote Sens. Environ.* **2017**, *189*, 84–95. [CrossRef]
28. Pan, C.G.; Kirchner, P.B.; Kimball, J.S.; Kim, Y.; Du, J. Rain-on-snow events in Alaska, their frequency and distribution from satellite observations. *Environ. Res. Lett.* **2018**, *13*, 075004. [CrossRef]
29. Kunzi, K.; Patil, S.; Rott, H. Snow-Cover Parameters Retrieved from Nimbus-7 Scanning Multichannel Microwave Radiometer (SMMR) Data. *IEEE Trans. Geosci. Remote Sens.* **1982**, *GE-20*, 452–467. [CrossRef]
30. WMO. *Review on Remote Sensing of the Snow Cover and on Methods of Mapping Snow*; World Meteorological Organization: Geneva, Switzerland, 2012.
31. Singh, G.; Yamaguchi, Y.; Park, S.E.; Venkataraman, G. Identification of Snow using SAR Polarimetry techniques. *Int. Arch. Photogramm. Remote Sens. Spat. Inf. Sci.* **2010**, *38 Pt 8*, 146–149.
32. Martini, A. Télédétection d'un Couvert Neigeux en Milieux Alpins à Partir de Données SAR Polarimétriques Multi-Fréquentielles et Multitemporelles. Ph.D. Thesis, Universite de Rennes, Rennes, France, 2005.
33. Magagi, R.; Bernier, M. Optimal conditions for wet snow detection using RADARSAT SAR data. *Remote Sens. Environ.* **2003**, *84*, 221–233. [CrossRef]
34. Marin, C.; Bertoldi, G.; Premier, V.; Callegari, M.; Brida, C.; Hürkamp, K.; Tschiersch, J.; Zebisch, M.; Notarnicola, C. Use of Sentinel-1 radar observations to evaluate snowmelt dynamics in alpine regions. *Cryosphere* **2020**, *14*, 935–956. [CrossRef]
35. Nagler, T.; Rott, H. Retrieval of wet snow by means of multitemporal SAR data. *IEEE Trans. Geosci. Remote Sens.* **2000**, *38*, 754–765. [CrossRef]
36. Rott, H.; Mätzler, C. Possibilities and limits of synthetic aperture radar for snow and glacier surveying. *Ann. Glaciol.* **1987**, *9*, 195–199. [CrossRef]
37. Antropova, Y.K.; Komarov, A.S.; Richardson, M.; Millard, K.; Smith, K. Detection of wet snow in the Arctic tundra from time-series fully-polarimetric RADARSAT-2 images. *Remote Sens. Environ.* **2022**, *283*, 113305. [CrossRef]
38. Donahue, C.; Hammonds, K. Laboratory Observations of Preferential Flow Paths in Snow Using Upward-Looking Polari-metric Radar and Hyperspectral Imaging. *Remote Sens.* **2022**, *14*, 2297. [CrossRef]
39. Nagler, T.; Rott, H.; Ripper, E.; Bippus, G.; Hetzenecker, M. Advancements for Snowmelt Monitoring by Means of Sentinel-1 SAR. *Remote Sens.* **2016**, *8*, 348. [CrossRef]
40. Idowu, A.N.; Marshall, H.-P. Snow Depth Retrieval from L-Band Data Based on Repeat Pass InSAR Techniques. In Proceedings of the IGARSS 2022—2022 IEEE International Geoscience and Remote Sensing Symposium, Kuala Lumpur, Malaysia, 17–22 July 2022; pp. 4248–4251. [CrossRef]
41. Snehmani; Venkataraman, G.; Nigam, A.K.; Singh, G. Development of an inversion algorithm for dry snow density estimation and its application with ENVISAT-ASAR dual co-polarization data. *Geocarto Int.* **2010**, *25*, 597–616. [CrossRef]
42. Kay, J.E.; Gillespie, A.R.; Hansen, G.B.; Pettit, E.C. Spatial relationships between snow contaminant content, grain size, and surface temperature from multispectral images of Mt. Rainier, Washington (USA). *Remote Sens. Environ.* **2003**, *86*, 216–231. [CrossRef]
43. Tonooka, H.; Watanabe, A. Applicability of Thermal Infrared Surface Emissivity Ratio for Snow/Ice Monitoring. In *SPIE 5655, Multispectral and Hyperspectral Remote Sensing Instruments and Applications II, Proceedings of the Fourth International Asia-Pacific Environmental Remote Sensing Symposium 2004: Remote Sensing of the Atmosphere, Ocean, Environment, and Space, Honolulu, Hawaii, USA, 8–12 November 2004*; Larar, A.M., Suzuki, M., Tong, Q., Eds.; Society of Photo Optical: Bellingham, WA, USA, 2005. [CrossRef]
44. Hori, M.; Aoki, T.; Tanikawa, T.; Motoyoshi, H.; Hachikubo, A.; Sugiura, K.; Yasunari, T.J.; Eide, H.; Storvold, R.; Nakajima, Y.; et al. In-situ measured spectral directional emissivity of snow and ice in the 8–14 μm atmospheric window. *Remote Sens. Environ.* **2006**, *100*, 486–502. [CrossRef]
45. Hori, M.; Aoki, T.; Tanikawa, T.; Kuchiki, K.; Niwano, M.; Yamaguchi, S.; Matoba, S. Dependence of Thermal Infrared Emissive Behaviors of Snow Cover on the Surface Snow Type. *Bull. Glaciol. Res.* **2014**, *320*, 33. [CrossRef]
46. Mishev, D. *Remote Earth Exploration from Space*; Bulgarian Academy of Sciences Publishing House: Sofia, Bulgaria, 1981; p. 206.
47. Available online: https://www.oruxmaps.com/cs/en/ (accessed on 27 April 2025).
48. Software Guide of "C-800 Utility" for C-800 SPECTROMETER. Available online: https://global.sekonic.com/downloads/?product=401-800 (accessed on 27 April 2025).
49. Ht-19 Thermal Camera Manual. Available online: https://hti-instrument.com/pages/ht-19-manual (accessed on 27 April 2025).

50. Available online: https://bg.benweilighting.com/info/cct-understanding-correlated-color-temperatur-84542133.html (accessed on 27 April 2025).
51. Available online: https://www.meteoswiss.admin.ch/weather/weather-and-climate-from-a-to-z/snow/types-of-snow.html (accessed on 27 April 2025).
52. Available online: https://compuweather.com/the-important-difference-between-wet-snow-and-dry-snow/ (accessed on 27 April 2025).
53. Available online: https://www.acurite.com/blogs/weather-101/types-of-snow?srsltid=AfmBOoowqd602gFqNOlIskJSchC5jnfhAd7LRCCtBn0Iw_6elXYd1gG9 (accessed on 27 April 2025).
54. Assenov, A. *Biogeography and Natural Capital of Bulgaria*; University Press St. Kliment Ohridski: Sofia, Bulgaria, 2021. (In Bulgarian)
55. Available online: http://www.journey.bg/bulgaria/bulgaria.php?guide=4338 (accessed on 27 April 2025).
56. Available online: https://sentinel.esa.int/web/sentinel/missions/sentinel-1 (accessed on 27 April 2025).
57. Karbou, F.; Veyssière, G.; Coleou, C.; Dufour, A.; Gouttevin, I.; Durand, P.; Gascoin, S.; Grizonnet, M. Monitoring Wet Snow Over an Alpine Region Using Sentinel-1 Observations. *Remote Sens.* **2021**, *13*, 381. [CrossRef]
58. Kropatsch, W.G.; Strobl, D. The generation of SAR layover and shadow maps from digital elevation models. *IEEE Trans. Geosci. Remote Sens.* **1990**, *28*, 98–107. [CrossRef]
59. Gelautz, M.; Frick, H.; Raggam, J.; Burgstaller, J.; Leberl, F. SAR image simulation and analysis of alpine terrain. *ISPRS J. Photogramm. Remote Sens.* **1998**, *53*, 17–38. [CrossRef]
60. Lillesand, T.M.; Kiefer, R.W. *Remote Sensing and Photo Interpretation*; John Wiley and Sons: New York, NY, USA, 1994; p. 750.
61. Available online: https://step.esa.int/main/download/snap-download (accessed on 27 April 2025).
62. Available online: https://step.esa.int/main/doc/tutorials/ (accessed on 27 April 2025).
63. Available online: https://step.esa.int/main/toolboxes/snap/ (accessed on 27 April 2025).
64. Available online: https://browser.stac.dataspace.copernicus.eu/collections/sentinel-1-grd?.language=en (accessed on 27 April 2025).
65. Pan, B.; Shi, X. Fusing Ascending and Descending Time-Series SAR Images with Dual-Polarized Pixel Attention UNet for Landslide Recognition. *Remote Sens.* **2023**, *15*, 5619. [CrossRef]
66. Available online: https://www.esri.com/en-us/arcgis/products/arcgis-pro/overview (accessed on 27 April 2025).
67. Available online: https://developers.planet.com/docs/data/planetscope/ (accessed on 27 April 2025).
68. Spasova, T.; Avetisyan, D. *Remote Sensing in Polar Regions Antarctic Part I, for Space Research and Technology Institute*; Bulgarian Academy of Sciences: Sofia, Bulgaria, 2024; ISBN 978-619-7490-19-0. 978-619-7490-14-5.
69. Available online: https://bgledfactory.bg/blog-article/44/kakvo-e-indeks-na-tsvetopredavane-cri.html (accessed on 27 April 2025).
70. Available online: https://lightingequipmentsales.com/cct-kelvin.html (accessed on 27 April 2025).
71. Available online: https://bg.benweilight.com/info/what-is-cct-how-to-choose-cct-for-led-lightin-69257544.html (accessed on 27 April 2025).
72. Available online: https://learn.leighcotnoir.com/artspeak/elements-color/hue-value-saturation (accessed on 27 April 2025).
73. Available online: https://en.wikipedia.org/wiki/Hue (accessed on 27 April 2025).
74. Available online: https://www.uprtek.com/en/blogs/what-is-tm-30-15-tm-30-18-and-should-i-use-it (accessed on 27 April 2025).
75. Available online: https://luminusdevices.zendesk.com/hc/en-us/articles/4421188803469-What-are-the-TM-30-18-Color-Rendition-Guidelines-Reports (accessed on 27 April 2025).
76. Spasova, T.; Avetisyan, D.; Stoyanov, A. Snow Cover Mapping Based on a Multi-Index Technique in Vitosha, Pirin and Rila mountains. In Proceedings of the SPIE 13197, Earth Resources and Environmental Remote Sensing/GIS Applications XV, 131971B, Edinburgh, UK, 16–20 September 2024. [CrossRef]
77. Available online: https://global.sekonic.com/sekonic-c-800-spectrometer/ (accessed on 27 April 2025).
78. Mätzler, C. Applications of the interaction of microwaves with the natural snow cover. *Remote Sens. Rev.* **1987**, *2*, 259–387. [CrossRef]
79. Rignot, E.; Echelmeyer, K.; Krabill, W. Penetration depth of interferometric synthetic-aperture radar signals in snow and ice. *Geophys. Res. Lett.* **2001**, *28*, 3501–3504. [CrossRef]
80. Langley, K.; Hamran, S.-E.; Hogda, K.A.; Storvold, R.; Brandt, O.; Hagen, J.O.; Kohler, J. Use of C-Band Ground Penetrating Radar to Determine Backscatter Sources Within Glaciers. *IEEE Trans. Geosci. Remote Sens.* **2007**, *45*, 1236–1246. [CrossRef]
81. Shi, J.; Dozier, J. Inferring snow wetness using C-band data from SIR-C's polarimetric synthetic aperture radar. *IEEE Trans. Geosci. Remote Sens.* **1995**, *33*, 905–914.
82. Mätzler, C.; Schanda, E. Snow mapping with active microwave sensors. *Int. J. Remote Sens.* **1984**, *5*, 409–422. [CrossRef]

83. Spasova, T. Polar digital space in Antarctica. In *Proceedings SPIE 12728, Proceedings of the Remote Sensing of the Ocean, Sea Ice, Coastal Waters, and Large Water Regions 2023, 127280P, Amsterdam, The Netherlands, 3–6 September 2023*; Bostater Jr., C.R., Neyt, X., Eds.; SPIE: Bellingham, WA, USA, 2023. [CrossRef]
84. Jiskoot, H. Glacier Surging. In *Encyclopedia of Snow, Ice and Glaciers*; Singh, V.P., Singh, P., Haritashya, U.K., Eds.; Springer: Dordrecht, The Netherlands, 2011; pp. 415–428, ISBN 978-9-04-812641-5.
85. Teleubay, Z.; Yermekov, F.; Tokbergenov, I.; Toleubekova, Z.; Igilmanov, A.; Yermekova, Z.; Assylkhanova, A. Comparison of Snow Indices in Assessing Snow Cover Depth in Northern Kazakhstan. *Sustainability* **2022**, *14*, 9643. [CrossRef]
86. Available online: https://hexagon.com/products/erdas-imagine (accessed on 27 April 2025).
87. Mardirosyan, G. *Natural Disasters and Ecological Catastrophes*; Bulgarian Academy of Sciences Publishing House: Sofia, Bulgaria, 2009.
88. Mardirosyan, G. *Fundamentals of Remote Aerospace Technologies*; New Bulgarian University: Sofia, Bulgaria, 2015; p. 238, ISBN 978-954-535-882-1.
89. Spasova, T.; Avetisyan, D. *A Synchronized Remote Sensing Monitoring Approach in the Livingstone is-Land Region of Antarctica, In Proceedings SPIE 12786, Proceedings of the Ninth International Conference on Remote Sensing and Geoinformation of the Environment (RSCy2023), 127861X, Ayia Napa, Cyprus, 3–5 April 2023*; Themistocleous, K., Hadjimitsis, D.G., Michaelides, S., Papadavid., G., Eds.; SPIE: Bellingham, WA, USA, 2023.
90. Borisova, D.; Hristova, V.; Dimitrov, V.M. Thematic Spectral Library for Remote Sensing Monitoring of Land Covers in Local Scale. In *Proceedings SPIE 11534, Proceedings of the Earth Resources and Environmental Remote Sensing/GIS Applications XI, 1153408 20–21 September 2020*; Schulz, K., Ed.; SPIE: Bellingham, WA, USA, 2020. [CrossRef]
91. Ohno, Y. CIE fundamentals for Color Measurements. In Proceedings of the Paper for IS&T NIP16 Conference, Vancouver, BC, Canada, 16–20 October 2000; pp. 540–545.
92. Borisova, D.; Kancheva, R.; Nikolov, H. Spectral Mixture Analysis of Land Covers. In Proceedings of the 25th EARSeL Symposium, Porto, Portugal, 6–11 June 2005; Global Developments in Environmental Earth Observation from Space. Millpress: Roterdam, The Netherlands, 2006; pp. 509–516.
93. Mishev, D. *Spectral Characteristics of Natural Objects*; Bulgarian Academy of Sciences Publishing House: Sofia, Bulgaria, 1986; p. 192.
94. Atanassov, V.; Jelev, G.; Kraleva, L. Imaging Spectrometer Data Correction. In Proceedings of the Scientific Conference with International Participation "Space, Ecology, Safety—SES'2005" Conference Proceedings, Book 1, Varna, Bulgaria, 10–13 June 2005; pp. 221–226.
95. Spasova, T. Creating a Digital Twin and Polar Digital space in Antarctica. In *Proceedings SPIE 12786, Ninth International Conference on Remote Sensing and Geoinformation of the Environment (RSCy2023), 12786, Ayia Napa, Cyprus, 3–5 April 2023*; SPIE: Bellingham, WA, USA, 2023. [CrossRef]
96. Ulaby, F.T.; Long, D.G.; Press, M. *Microwave Radar and Radiometric Remote Sensing*; Ulaby, F.T., Ed.; The University of Michigan Press: Ann Arbor, MI, USA, 2014.
97. Dasser, G.; Bickel, V.T.; Rüetschi, M.; Jacquemart, M.; Bavay, M.; Hafner, E.D.; van Herwijnen, A.; Manconi, A. Moni-Toring Snow Wetness Evolution from Satellite with Sentinel-1 Multi-Track Composites, EGUsphere 2024. Available online: https://egusphere.copernicus.org/preprints/2024/egusphere-2024-1510/ (accessed on 27 April 2025).
98. Beltramone, G.; Frery, A.C.; Rotela, C.; Germán, A.; Bonansea, M.; Scavuzzo, C.M.; Ferral, A. Identification of Seasonal Snow Phase Changes from C-Band SAR Time Series with Dynamic Thresh-olds. *IEEE J. Sel. Top. Appl. Earth Obs. Remote Sens.* **2023**, *16*, 6995–7008. [CrossRef]
99. Spasova, T.; Nedkov, R. Monitoring of Short-Lived Snow Coverage by Radar and Optical Data from Sentinel-1 and Sentinel-2 Satellites. *Ecol. Eng. Environ. Prot.* **2017**, *2*, 13–19. [CrossRef]
100. Spasova, T.; Dancheva, A.; Avetisyan, D.; Ivanova, I.; Popov, I.; Shirov, B. Monitoring of renewable energy sources with remote sensing, open data, and field data in Bulgaria. In Proceedings of the SPIE 12733, Image and Signal Processing for Remote Sensing XXIX, 1273311, Amsterdam, The Netherlands, 4–5 September 2023; SPIE: Bellingham, WA, USA, 2023. [CrossRef]

Disclaimer/Publisher's Note: The statements, opinions and data contained in all publications are solely those of the individual author(s) and contributor(s) and not of MDPI and/or the editor(s). MDPI and/or the editor(s) disclaim responsibility for any injury to people or property resulting from any ideas, methods, instructions or products referred to in the content.